

A MEASUREMENT OF THE KINETIC SUNYAEV-ZEL'DOVICH SIGNAL TOWARD MACS J0717.5+3745

J. SAYERS^{1,2,12}, T. MROCKOWSKI^{1,3,4}, M. ZEMCOV^{1,3}, P. M. KORNGUT³, J. BOCK^{1,3}, E. BULBUL⁵, N. G. CZAKON¹, E. EGAMI⁶, S. R. GOLWALA¹, P. M. KOCH⁷, K.-Y. LIN⁷, A. MANTZ⁸, S. M. MOLNAR⁹, L. MOUSTAKAS³, E. PIERPAOLI¹⁰, T. D. RAWLE⁶, E. D. REESE¹¹, M. REX⁶, J. A. SHITANISHI¹⁰, S. SIEGEL¹, & K. UMETSU⁷

Draft version December 16, 2013

ABSTRACT

We report our analysis of MACS J0717.5+3745 using 140 and 268 GHz Bolocam data collected at the Caltech Submillimeter Observatory. We detect extended Sunyaev-Zel'dovich (SZ) effect signal at high significance in both Bolocam bands, and we employ *Herschel*-SPIRE observations to subtract the signal from dusty background galaxies in the 268 GHz data. We constrain the two-band SZ surface brightness toward two of the sub-clusters of MACS J0717.5+3745: the main sub-cluster (named C), and a sub-cluster identified in spectroscopic optical data to have a line-of-sight velocity of +3200 km s⁻¹ (named B). We determine the surface brightness in two separate ways: via fits of parametric models and via direct integration of the images. For both sub-clusters, we find consistent surface brightnesses from both analysis methods. We constrain spectral templates consisting of relativistically corrected thermal and kinetic SZ signals, using a jointly-derived electron temperature from *Chandra* and *XMM-Newton* under the assumption that each sub-cluster is isothermal. The data show no evidence for a kinetic SZ signal toward sub-cluster C, but they do indicate a significant kinetic SZ signal toward sub-cluster B. The model-derived surface brightnesses for sub-cluster B yield a best-fit line-of-sight velocity of $v_z = +3450 \pm 900$ km s⁻¹, with $(1 - \text{Prob}[v_z \geq 0]) = 1.3 \times 10^{-5}$ (4.2 σ away from 0 for a Gaussian distribution). The directly integrated sub-cluster B SZ surface brightnesses provide a best-fit $v_z = +2550 \pm 1050$ km s⁻¹, with $(1 - \text{Prob}[v_z \geq 0]) = 2.2 \times 10^{-3}$ (2.9 σ).

Subject headings: galaxies: clusters: intracluster medium — galaxies: clusters: individual: (MACS J0717.5+3745)

1. INTRODUCTION

Measurements of large-scale peculiar velocities provide a direct probe of cosmological models and can be used to place constraints on parameters that are highly degenerate and/or unconstrained via other cosmological probes, such as measurements of primary CMB fluctuations (Bennett et al. 2012; Hinshaw et al. 2012; Planck Collaboration et al. 2013b,c) and supernovae distance measurements (Conley et al. 2011; Suzuki et al. 2012). Specifically, these peculiar velocities depend on the properties and distributions of large-scale structure, along with the characteristics of dark energy and the behavior of gravity on the corresponding length scales. Con-

sequently, peculiar velocity measurements for large numbers of objects can probe the redshift evolution of the properties of dark energy (Bhattacharya & Kosowsky 2008) and also distinguish between dark energy and modified gravity models (Kosowsky & Bhattacharya 2009). In addition, measurements of an extremely large peculiar velocity for a single object (e.g., 1E0657-56, also known as the bullet cluster) can be used to directly test the validity of standard cosmological models (Hayashi & White 2006; Lee & Komatsu 2010; Thompson & Nagamine 2012).

In the local universe, line-of-sight peculiar velocities can be measured using a combination of spectroscopy and distance measurements via the extragalactic distance ladder, generally using the relation described by Tully & Fisher (1977). Such measurements have been used to constrain cosmological parameters like the total matter density Ω_m and the normalization of density fluctuations σ_8 , generally finding good agreement with other cosmological probes (e.g., Feldman et al. 2010; Nusser & Davis 2011; Ma et al. 2012). Unfortunately, uncertainties in the extragalactic distance ladder are proportional to distance, therefore preventing the application of these methods outside the local universe. In contrast, the kinetic Sunyaev-Zel'dovich (SZ) effect provides a direct measurement of the line-of-sight peculiar velocity of the distribution of hot electrons within galaxy clusters (Sunyaev & Zel'dovich 1972, See Section 2). In addition, the surface brightness of the kinetic SZ signal is independent of redshift, depending only on the electron optical depth and line-of-sight peculiar velocity. Consequently, many groups have performed detailed studies of

¹ Division of Physics, Math, and Astronomy, California Institute of Technology, 1200 East California Blvd, Pasadena, CA 91125

² Norris Foundation CCAT Postdoctoral Fellow

³ Jet Propulsion Laboratory, 4800 Oak Grove Drive, Pasadena, CA 91109

⁴ NASA Einstein Postdoctoral Fellow

⁵ Harvard-Smithsonian Center for Astrophysics, 60 Garden Street, Cambridge, MA 02138

⁶ Steward Observatory, University of Arizona, 933 North Cherry Avenue, Tucson, AZ 85721

⁷ Institute of Astronomy and Astrophysics, Academia Sinica, P.O. Box 23-141, Taipei 10617, Taiwan

⁸ Kavli Institute for Cosmological Physics, University of Chicago, 5640 South Ellis Avenue, Chicago, IL 60637

⁹ LeCosPA Center, National Taiwan University, Taipei 10617, Taiwan

¹⁰ Department of Physics and Astronomy, University of Southern California, 3620 McClintock Avenue, Los Angeles, CA 90089

¹¹ Department of Physics and Astronomy, University of Pennsylvania, 209 South 33rd Street, Philadelphia, PA 19104

¹² jack@caltech.edu

the cosmological constraints that would be possible with large-scale peculiar velocity surveys using the kinetic SZ signal (e.g., Bhattacharya & Kosowsky 2008; Kosowsky & Bhattacharya 2009; Mak et al. 2011).

Despite the great promise of kinetic SZ surveys, measurements of the kinetic SZ signal have proven to be a significant observational challenge. Over the past two decades, several attempts have been made to detect the kinetic SZ signal toward a variety of individual massive clusters. These observational efforts have used a range of instrumentation, including: the dedicated multi-band photometer SuZIE and its successors (Holzapfel et al. 1997; Benson et al. 2003), multi-band data collected from a range of facilities (Kitayama et al. 2004), the moderate resolution spectroscopic receiver Z-Spec (Zemcov et al. 2012), and the two-band photometric imaging camera Bolocam (Mauskopf et al. 2012; Mroczkowski et al. 2012). None of these observations have made a high-significance detection of the kinetic SZ signal, and the derived uncertainties on the line-of-sight peculiar velocities have not improved significantly from the first measurements with SuZIE, at least in part because none of the subsequent measurements have used instrumentation specifically designed to detect the kinetic SZ signal.

Recently, data from the *WMAP* and *Planck* satellites have been used to place upper limits on bulk flows and rms variations in peculiar velocities via the kinetic SZ signal (Osborne et al. 2011; Planck Collaboration et al. 2013d). In addition, Hand et al. (2012) used a combination of Atacama Cosmology Telescope (ACT) and Sloan Digital Sky Survey III data to constrain the mean pairwise momentum of clusters using a kinetic SZ signature that is inconsistent with noise at a confidence level of 99.8%. Furthermore, upper limits on the kinetic SZ power spectrum measured by the South Pole Telescope (SPT) have been used to inform cosmological simulations and to place constraints on the reionization history of the universe (Reichardt et al. 2012; Zahn et al. 2012).

One of the strongest hints of a kinetic SZ detection was presented in Mroczkowski et al. (2012, hereafter M12) toward the massive cluster MACS J0717.5+3745 using Bolocam measurements at 140 and 268 GHz. Motivated by this result, we have collected a significant amount of additional 268 GHz Bolocam data toward this cluster. The results we obtain using this additional, deeper data are presented in this manuscript, which is organized as follows. In Section 2 we present the SZ effect and in Section 3 we describe previous analyses of MACS J0717.5+3745. In Section 4 we provide the details of our data reduction. We describe our model of the SZ signal toward MACS J0717.5+3745 in Section 5 and provide the corresponding constraints on the two-band SZ surface brightnesses of the cluster in Sections 6 and 7. In Section 8 we give the line-of-sight peculiar velocity constraints derived from these surface brightnesses, in Section 9 we put these results in a broader context, and in Section 10 we briefly summarize our analysis. We also include an Appendix which fully details our treatment of the cosmic infrared background (CIB) in the 268 GHz data.

2. THE SZ EFFECT

When a massive galaxy cluster is moving with respect to the rest frame of the CMB, the Doppler-induced spec-

tral distortion of the CMB due to the bulk motion of the electrons in the intra-cluster medium (ICM) is described by the kinetic SZ effect (e.g., Sunyaev & Zel'dovich 1972; Birkinshaw 1999; Carlstrom et al. 2002). The change in CMB temperature due to the kinetic SZ effect is given by

$$\frac{\Delta T_{CMB}}{T_{CMB}} = -\frac{v_z}{c}\tau_e, \quad (1)$$

where v_z is the ICM peculiar velocity along the line-of-sight, c is the speed of light, and τ_e is the total electron optical depth

$$\tau_e = \int n_e \sigma_T dl, \quad (2)$$

for an electron density n_e integrated along the line of sight dl (σ_T is the Thompson cross section). We note that a positive peculiar velocity results in a negative temperature change, under the convention that a Doppler shift toward higher redshift corresponds to a positive value of v_z . In addition, we note that there are small relativistic corrections to the kinetic SZ signal (e.g., Nozawa et al. 1998a; Sazonov & Sunyaev 1998; Nozawa et al. 2006; Chluba et al. 2012).

There is also a thermal SZ effect, which describes the Compton scattering of CMB photons off of high energy electrons in the ICM of massive clusters (e.g., Sunyaev & Zel'dovich 1972; Rephaeli 1995a; Birkinshaw 1999; Carlstrom et al. 2002). Specifically, the change in CMB temperature due to the thermal SZ effect is given by

$$\frac{\Delta T_{CMB}}{T_{CMB}} = f(\nu, T_e)y, \quad (3)$$

where $f(\nu, T_e)$ encodes the frequency ν dependence, including relativistic corrections that depend on the electron temperature T_e (e.g., Rephaeli 1995b; Itoh et al. 1998; Nozawa et al. 1998b; Itoh & Nozawa 2004; Chluba et al. 2012) and

$$y = \int n_e \sigma_T \frac{k_B T_e}{m_e c^2} dl \quad (4)$$

(k_B is Boltzmann's constant and m_e is the electron mass). In the limit of an isothermal distribution, y is directly and linearly proportional to the total electron optical depth τ_e .

3. PREVIOUS ANALYSES OF MACS J0717.5+3745

MACS J0717.5+3745, located at $z = 0.55$, was discovered as part of the Massive Cluster Survey (MACS, Ebeling et al. 2001, 2007), and is extremely massive and dynamically disturbed. As such, it has been the focus of many studies at a range of wavelengths, and it has been chosen as part of the six-cluster Hubble Space Telescope Frontier Fields program.¹³ Radio observations have shown that MACS J0717.5+3745 hosts the most powerful radio halo known (Edge et al. 2003; van Weeren et al. 2009; Bonafede et al. 2009), and strong lensing data have shown that MACS J0717.5+3745 has the largest known Einstein radius (Zitrin et al. 2009; Meneghetti et al. 2011; Waizmann et al. 2012). From both the galaxy distribution (Ebeling et al. 2004), and weak lensing studies (Jauzac et al. 2012; Medezinski et al. 2013), MACS

¹³ <http://www.stsci.edu/hst/campaigns/frontier-fields/>

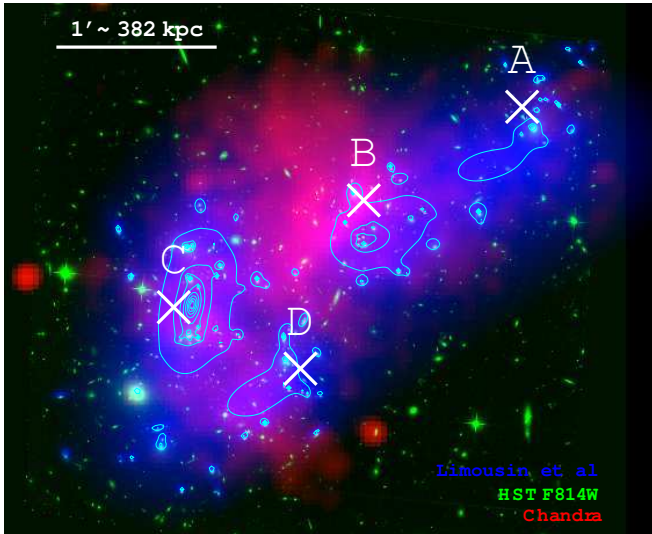


FIG. 1.— False-color composite image of MACS J0717.5+3745 with the lensing results of Limousin et al. (2012) in blue, the Hubble Space Telescope image using the F814W filter in green, and the *Chandra* X-ray image in red. The blue contours show the Limousin et al. (2012) result on a linear scale, and clearly indicate the four sub-clusters labeled A through D, with white Xs marking the sub-cluster positions determined by Ma et al. (2009) from the galaxy distribution.

J0717.5+3745 also appears to be part of a large, extended filamentary structure. In addition, it has the highest X-ray temperature among all of the clusters in the MACS catalog (Ebeling et al. 2007).

Ma et al. (2009) performed a joint analysis using X-ray data, along with the measured galaxy positions and redshifts, and identified four distinct sub-clusters in MACS J0717.5+3745, from N to S labeled as A, B, C, and D (see Figure 1). An independent strong lensing analysis described in Limousin et al. (2012) also identified four sub-clusters, with similar positions to the ones given in Ma et al. (2009). Both analyses found sub-cluster C to be the most massive system, and Ma et al. (2009) determined that sub-cluster C is probably the highly disturbed core of the main system. Sub-clusters B and D are assumed to be relatively intact cores of systems that are merging along a direction close to the line-of-sight. In particular, sub-cluster B is coincident with an X-ray temperature that is colder than the surrounding regions, indicating that its core has not been highly disrupted by the merger. From the spectroscopic data, Ma et al. (2009) found that sub-cluster B has a line-of-sight velocity that differs from the other components by approximately 3000 km s^{-1} . Further indications of this large line-of-sight velocity for sub-cluster B were presented in M12, who found a similar best-fit velocity by using X-ray and SZ measurements to constrain the kinetic SZ signal toward that sub-cluster, although the statistical significance of their kinetic SZ constraint on the velocity is modest ($\simeq 2\sigma$). This wide range of observational data toward MACS J0717.5+3745 is therefore converging to what appears to be a coherent picture of this complex system.

4. DATA REDUCTION

4.1. *Bolocam*

We observed MACS J0717.5+3745 with *Bolocam* from the Caltech Submillimeter Observatory (CSO) for a total of 12.5 hours at 140 GHz and for a total of 27.3 hours at 268 GHz, where the effective band centers are quoted for a CMB spectrum. Compared to the previous *Bolocam* analysis presented in M12, this represents an additional 19.3 hours of data collected at 268 GHz in 2012 December. In contrast to the original 8.0 hours of 268 GHz integration used in M12, much of which was collected in poor observing conditions with a 225 GHz optical depth $\tau_{225} > 0.10$, most of the additional 19.3 hours of 268 GHz integration was obtained with $\tau_{225} \simeq 0.05$. This additional data was therefore collected during the lowest opacity conditions generally available from the CSO.

The *Bolocam* instrument has an $8'$ diameter circular field of view (FOV), and point-spread functions (PSFs) that are approximately Gaussian with full-widths at half-maximums (FWHMs) equal to $58''$ and $31''$ at 140 and 268 GHz, respectively (Glenn et al. 2002; Haig et al. 2004). All of our *Bolocam* observations of MACS J0717.5+3745 involved scanning the CSO in a Lissajous pattern with an RMS velocity of approximately $4'$ /sec. The details of our data reduction are given elsewhere (Sayers et al. 2011, M12), and we briefly summarize our procedure below.

First, we obtain pointing corrections accurate to $5''$ using frequent observations of nearby quasars, and we obtain an absolute flux calibration accurate to 5% and 10% at 140 and 268 GHz, respectively, using observations of Uranus and Neptune (Griffin & Orton 1993; Sayers et al. 2012). We note that Hasselfield et al. (2013) recently determined the brightness temperature of Uranus to be $106.7 \pm 2.2 \text{ K}$ at 149 GHz using ACT observations calibrated against the primary CMB anisotropies measured by the *WMAP* satellite. Also, Planck Collaboration et al. (2013a) recently determined the brightness temperature of Uranus to be $108.4 \pm 2.9 \text{ K}$ at 143 GHz based on *Planck* data. Our calibration model assumes a brightness temperature of $106.6 \pm 3.5 \text{ K}$ for the 140 GHz *Bolocam* band-pass, which was measured in Sayers et al. (2012) by extrapolating the *WMAP* 94 GHz brightness measurements presented in Weiland et al. (2011) using the model of Griffin & Orton (1993). This model predicts the brightness temperature of Uranus to increase with decreasing frequency. As a result, the ACT and *Planck* measurements imply a best-fit 140 GHz brightness temperature that is approximately 2.5 K higher than our assumed value of 106.6 K. However, this difference is comparable to the ACT and *Planck* measurement uncertainties, and it is well below our estimated 5% flux calibration uncertainty at 140 GHz. We therefore have not updated our calibration model. Furthermore, we note that the accuracy of the ACT and *Planck* Uranus brightness temperatures is 2 – 3%, which is only slightly smaller than the 3.3% accuracy of our assumed 140 GHz brightness temperature. Furthermore, our 140 GHz calibration uncertainty receives an approximately equal contribution from our 3.1% beam solid angle uncertainty. Revising our flux calibration using ACT and *Planck* would thus not have a significant effect on our overall calibration uncertainty, which itself is already sub-dominant to measurement uncertainties (see Table 2). Finally, we note that our 10% flux calibration at 268 GHz is limited largely by atmospheric fluctuations, and therefore a more accurate

Uranus brightness temperature at that frequency would have no effect on our overall calibration uncertainty.

To remove atmospheric fluctuations from the data, we first subtract a template of the common mode signal over the FOV, and we then high-pass filter (HPF) the time-stream data at 250 and 500 mHz at 140 and 268 GHz, respectively. The large amplitude of the atmospheric fluctuations in the 268 GHz data necessitates this more aggressive HPF, and this filtering represents a slight change from the M12 analysis, which used a 250 mHz HPF for both datasets. We used a scan speed of $\simeq 4'$ /sec for our observations, and the HPFs at 250 or 500 mHz therefore correspond to angular scales of $16'$ and $8'$, respectively. Consequently, the maximum angular scale preserved by our filtering is largely set by the common mode subtraction over Bolocam's $8'$ FOV. Because our processing removes astronomical signals with angular sizes larger than the $8'$ FOV, we determine the map-space transfer function at each wavelength by reverse-mapping and processing an image template through the entire reduction pipeline. We estimate the instrumental and atmospheric noise in our images by forming 1000 separate jackknife realizations of the data, where a randomly selected subset of half the single observations is multiplied by -1 to remove all astronomical signals. There are 75 single 10-minute observations of MACS J0717.5+3745 at 140 GHz and 164 single 10-minute observations of MACS J0717.5+3745 at 268 GHz.

To account for noise from unwanted astronomical signals, we first add a different random realization of the primary cosmic microwave background (CMB) fluctuations, using the power spectrum measurements from the South Pole Telescope (SPT), to each jackknife (Reichardt et al. 2012; Story et al. 2012). At 140 GHz, we add an additional random realization of the CIB, again based on the measured SPT power spectra (Hall et al. 2010), under the assumption that the fluctuations are Gaussian. This assumption is not strictly true, but the CIB fluctuations are more than an order of magnitude dimmer than the other noise fluctuations in the data, and therefore a breakdown of this assumption is not likely to have a noticeable effect on our results. The CIB is significantly brighter at 268 GHz, and we therefore use a much more detailed model to account for it in those data, as described in the Appendix. Throughout this manuscript we refer to these 1000 jackknife plus astronomical noise realizations as “noise realizations”.

For the analyses described in this manuscript, we make use of the Bolocam data in two different ways. We use images of the processed data, which cover a maximum size of $14' \times 14'$, to constrain parametric models of the astronomical signals (see Section 5). This analysis involves convolving the model with the signal transfer function of the data processing and the Bolocam PSF. To determine best-fit parameters for a given model, we use the generalized least squares fitting algorithm MPFIT-FUN (Markwardt 2009) under the simplifying assumption that the map noise covariance matrix is diagonal. We have demonstrated that this fitting method produces unbiased estimates of the best-fit parameter values (Sayers et al. 2011), although in some cases it does produce a slightly biased estimate of the uncertainties on these best-fit parameters. Therefore, to fully account for all of the subtleties of our noise, we derive all of the parameter

uncertainties via the spread of best-fit values we obtain from applying the same fitting algorithm to a sample of 1000 noise plus signal realizations. Each noise plus signal realization is generated by adding a noise realization to the best-fit model found for the real data.

We also deconvolve the transfer function of the data processing to obtain unbiased images after first reducing the image to a maximum size of $10' \times 10'$ to prevent significant amplification of the noise on the largest angular scales. One subtlety in this process is the fact that the signal transfer function is equal to 0 at an angular wavenumber of 0 (i.e., the DC signal level of the image is unconstrained). We therefore use the parametric model fits to constrain the DC signal level, as described in Section 6.1. As a result, the deconvolved images have some model dependence. Consequently, to ensure that the uncertainties on the model accurately represent the underlying uncertainties on the data, both for the model fits alone and for the results derived from the deconvolved images, the model must provide an acceptable fit quality. By requiring a model with an acceptable fit quality, we also ensure that the results derived from model fits will be consistent with those derived from the deconvolved images. To estimate the noise in the deconvolved images, we also deconvolve the transfer function from each of the 1000 noise realizations.

4.2. *Chandra*

Our analysis of the *Chandra* X-ray exposures of MACS J0717.5+3745 is nearly identical to the analysis described in M12, and we briefly summarize the main aspects below. As in M12, we utilize both *Chandra* ACIS-I X-ray observations of MACS J0717.5+3745 (Obs IDs 1655 and 4200), for a total exposure time of 81 ksec (see Reese et al. (2010) for the reduction details). From these X-ray data we compute pseudo-pressure

$$P_e = n_e k_B T_e \simeq \sqrt{\frac{4\pi(1+z)^3 S_X}{l \Lambda_{ee}(T_e, Z)}} k_B T_e, \quad (5)$$

where S_X is the X-ray surface brightness

$$S_X = \frac{1}{4\pi(1+z)^3} \int n_e^2 \Lambda_{ee}(T_e, Z) dl, \quad (6)$$

l is the effective line-of-sight extent of the ICM, and $\Lambda_{ee}(T_e, Z)$ is the X-ray emissivity as a function of T_e and metallicity Z . To generate pseudo-pressure maps from the *Chandra* images, we first bin the data using *contbin* (Sanders 2006). We construct the pseudo-pressure maps from T_e maps generated by computing T_e within each bin and n_e maps computed from the X-ray surface brightness (see Equation 5). To rescale the pseudo-pressure maps to units of Compton- y , we need to determine the value of l (which in M12 was done using 31 GHz SZA data, but in practice is left as a free parameter in all of our fits). This X-ray template for the thermal SZ signal, which is simply a rescaling of the X-ray pseudo-pressure map, is called a “pseudo Compton- y map” throughout this manuscript. For consistency with M12, we employ the same pseudo Compton- y map that was generated for that analysis. We note that this map was generated using CIAO version 4.3 and calibration database (CALDB) version 4.4.5 (Fruscione et al. 2006).

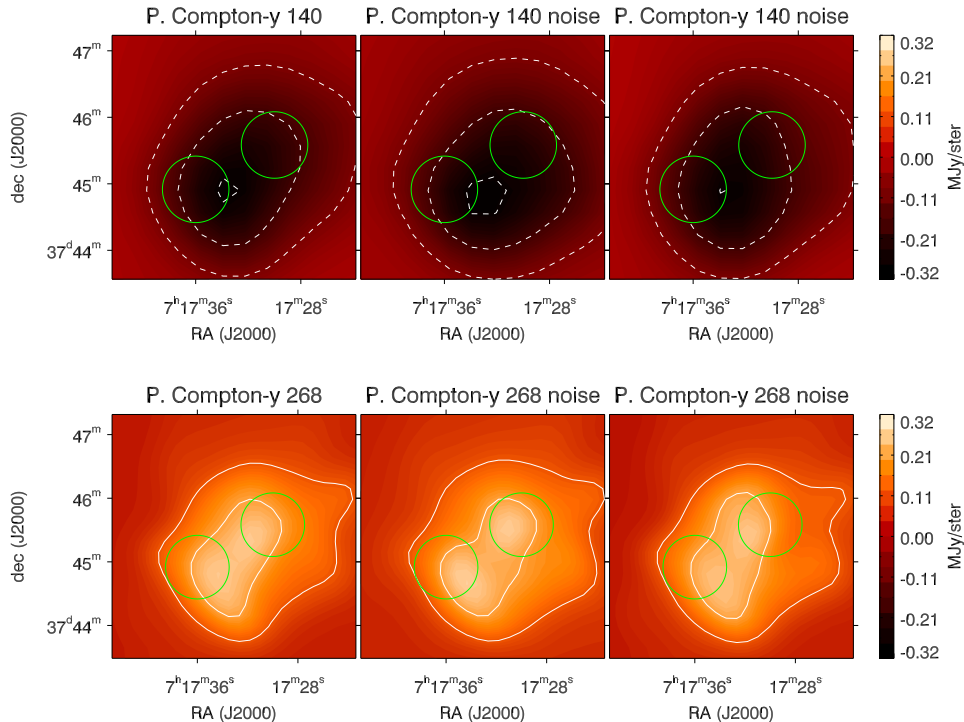


FIG. 2.— Thumbnails of the pseudo Compton- y maps we derive from the *Chandra* X-ray data. From left to right, the thumbnails show the best-fit map and two realizations based on the X-ray measurement uncertainties. The top row shows the maps at 140 GHz, and the bottom row shows the maps at 268 GHz. In both cases, the maps are convolved with the Bolocam PSF at the respective frequency. The white contours are spaced by 0.10 MJy sr^{-1} , with solid representing positive values and dashed representing negative values. The $1'$ diameter apertures centered on sub-cluster C (lower left) and sub-cluster B (upper right) are shown in green. Note that the approximate conversion factor from MJy sr^{-1} to y is -1×10^{-3} at 140 GHz and $+1 \times 10^{-3}$ at 268 GHz.

New for this analysis compared to M12, we also generate 20 realizations of the pseudo Compton- y map that are fluctuated by the X-ray measurement uncertainties on T_e , which dominate the uncertainty of the pseudo-pressure maps (see Figure 2). We note that, in addition to measurement uncertainties, the pseudo Compton- y maps are also subject to possible systematic errors due to gas clumping within the ICM. Clumping is defined as

$$C = \frac{\langle n_e^2 \rangle}{\langle n_e \rangle^2}, \quad (7)$$

and from the equations listed above, we see that the pseudo-Compton- y maps are sensitive to \sqrt{C} . Typical clumping factors of $C \simeq 1.1 - 1.2$ within R_{500} are expected from simulations (e.g., Zhuravleva et al. 2013). Assuming clumping is uncorrelated with temperature variations, clumping is sub-dominant to the variations included in the input temperature maps, and we therefore do not include any additional uncertainty from clumping in our 20 realizations of the pseudo Compton- y maps. In addition, we note that the average systematic trend for X-ray surface brightness to be boosted by clumping is mitigated by the fact that the amplitude of the Compton- y maps is constrained by the SZ data via the factor of l .

We also use the *Chandra* data to constrain the electron temperature T_e within two $1'$ diameter regions centered on sub-clusters B and C (these temperatures are applied to our analysis in Section 8). In contrast to the pseudo Compton- y maps, which we obtain via the same reduction that was used in M12, we constrain these values of T_e using maps generated with CIAO version 4.5 and

calibration database (CALDB) version 4.5.6 (Fruscione et al. 2006). We fit the temperatures and metallicities of the regions in XSPEC (Dorman & Arnaud 2001) using the Astrophysical Plasma Emission Code (APEC) model (Smith et al. 2001). We find $T_e = 13.8_{-1.3}^{+1.6}$ keV for sub-cluster B and $T_e = 24.4_{-3.8}^{+7.8}$ keV for sub-cluster C, using the extended C-statistic to determine the temperature likelihoods.¹⁴

4.3. *XMM-Newton*

To better constrain the electron temperatures of sub-clusters B and C, we make use of $\simeq 200$ ksec of *XMM-Newton* X-ray data toward MACS J0717.5+3745. These data became public in 2012 October (Obs Ids; 0672420101, 0672420301, 0672420301), and therefore were not included in M12. We perform the *XMM* MOS data processing and background modeling with the *XMM* Extended Source Analysis Software (*ESAS*) using the methods reported in Kuntz & Snowden (2008) and Snowden et al. (2008). The details of our *XMM* analysis are described fully in Bulbul et al. (2012), and we provide a summary and discuss important differences here.

Our *XMM-Newton* data analysis includes production of the calibrated event files, filtering for the high intensity soft proton flares, and determination of the back-

¹⁴ Our uncertainties on the *Chandra*-derived temperature of sub-cluster B are significantly lower than the values reported in Table 3 of M12. This is due to the fact that our current analysis uses a $1'$ diameter region, while the M12 analysis used a $40''$ diameter region (both analyses use a $1'$ diameter region for sub-cluster C). There are additional $< 5\%$ differences due to the updated calibration we use for our current analysis.

ground intensity in each observation. The net exposure time after filtering the event files for good time intervals is 155 ksec. Given the superior spatial resolution of *Chandra*, we use both *Chandra* and *XMM* to identify regions contaminated by extragalactic X-ray sources not associated with the cluster gas. Excluding these regions, we extract spectra using $1'$ diameter regions centered on sub-clusters B and C, identical to the regions we use for the *Chandra* analysis. The temperature gradient is not large, and so contamination by adjacent regions (e.g., other sub-clusters) due to the wider PSF of *XMM* should not affect the extracted temperature for each region.

For each extracted spectrum, we model a superposition of four main background components: quiescent particle background, soft X-ray background emission (including solar wind charge exchange, Galactic halo, local hot bubble, and extragalactic unresolved sources), and residual contamination from soft protons (Kuntz & Snowden 2008). As in Snowden et al. (2008), we model the contamination due to unresolved point sources using an absorbed power law component with spectral index $\alpha = 1.46$ and normalization = 8.88×10^7 photons $\text{keV}^{-1} \text{cm}^{-2} \text{s}^{-1}$ at 1 keV.

We simultaneously fit all of the EPIC-MOS spectra using the energy range 0.3–10.0 keV. As with the *Chandra* spectral analysis, we use the absorbed APEC model to fit the cluster emission, employing the extended C-statistic for our likelihood analysis within each sub-cluster region.

From the *XMM* data, we find $T_e = 10.8_{-0.5}^{+0.5}$ keV for sub-cluster B and $T_e = 18.6_{-1.4}^{+1.6}$ keV for sub-cluster C. We note that these values are $\simeq 25\%$ lower than the electron temperatures we derive from the *Chandra* data. This systematic difference at high temperature is consistent with previous comparisons between *XMM* and *Chandra* (e.g., Nevalainen et al. 2010; Li et al. 2012; Mahdavi et al. 2013), although we note that, in our case, the statistical significance of the difference is relatively small ($\lesssim 2\sigma$). We consequently choose to combine the temperature measurements from the two X-ray observatories, and we obtain maximum likelihood values of $T_e = 11.4_{-0.5}^{+0.5}$ keV for sub-cluster B and $T_e = 19.9_{-1.4}^{+1.5}$ keV for sub-cluster C. We explore the impact of using this joint temperature constraint, rather than the constraint from either *XMM* or *Chandra* individually, in Section 9.2.

5. MODEL OF THE SZ SIGNAL

In order to model the SZ signals from the ICM of MACS J0717.5+3745, we employ the pseudo Compton- y map to describe the overall shape of the thermal SZ signal. The X-ray data we use to create the pseudo Compton- y map depend negligibly on the line-of-sight velocity of the ICM, and the map therefore provides a spatial template for the thermal SZ signal that is free from contamination from the kinetic SZ signal. We then convert this map to units of surface brightness in each Bolocam observing band according to the thermal SZ equations (Sunyaev & Zel'dovich 1972), including relativistic corrections (Itoh et al. 1998; Nozawa et al. 1998b,a; Itoh & Nozawa 2004). For this conversion we compute the responsivity-weighted average bandpass over all the Bolocam detectors, and from this spectrum we determine the effective band center for a thermal SZ spectrum. Due to relativistic corrections, this effective

band center depends on the ICM temperature. For the 140 GHz band, both the thermal and kinetic SZ band centers are $\simeq 140$ GHz, while the 268 GHz thermal SZ band center is $\simeq 275$ GHz and the kinetic SZ band center is $\simeq 268$ GHz. Then, for each Bolocam band, we convolve the pseudo Compton- y map with both the Bolocam PSF and the transfer function of the data processing.

We first constrain the normalization of the pseudo Compton- y map via a simultaneous fit to both the 140 and 268 GHz Bolocam data. Physically, this corresponds to a constraint on the effective line-of-sight extent of the ICM l , under the assumption of zero kinetic SZ signal. For this fit, we use only the data within a $4' \times 4'$ square region approximately centered on the peak of the SZ signal at 140 GHz. We choose this region because it is large enough to contain the bulk of the SZ signal and it is small enough to mitigate the effects of the large-angular-scale atmospheric noise in the 268 GHz data. The quality of this fit is very poor, with a $\chi^2 = 853.4$ for 717 degrees of freedom, indicating that the pseudo Compton- y map alone is inadequate to describe our Bolocam SZ data (see Figure 3).

Motivated by this poor fit, along with the significant differences in the line-of-sight velocities measured by Ma et al. (2009) for the four identified sub-clusters in MACS J0717.5+3745, and the results from M12, we consider additional components to our model of the ICM. To determine which, if any, additional model components are required in order to describe the data, we perform a simulated F-test according to the procedure described in Czakon (2013). To perform this test we first insert the baseline model into each of our 1000 noise realizations (in this case the baseline model is the pseudo Compton- y map with our best-fit single normalization). We then fit two models to each of these realizations, one consisting of only the baseline model, and one with an extension to the baseline model. We compute the value of $\Delta\chi^2$ from these two separate fits for each of the 1000 realizations, and the resulting values provide a measurement of the distribution of $\Delta\chi^2$ for the null hypothesis that the model extension is not required by the data.

There are several possible model extensions to consider, and we therefore proceed according to the following decision tree: 1) determine the value of $\Delta\chi^2$ separately for each possible model extension; 2) perform the simulated F-test to determine which extension is most preferred by the data; 3) if the most preferred model extension is preferred at a high enough significance, which we quantify based on a probability to exceed (PTE) from the simulated F-test, then the model extension is added to the baseline model. These steps are repeated until none of the possible model extensions have a simulated F-test PTE below our threshold, which we have chosen to be equal to 0.02.¹⁵

As a first possible model extension, we consider a smooth template of the SZ signal centered on one of the

¹⁵ As we describe below, we consider 5 independent potential model extensions, and consequently a possible total of $2^5 = 32$ model permutations. Our PTE threshold, which is necessarily somewhat arbitrary, is therefore small enough to ensure that a random fluctuation among this set of 32 permutations is unlikely to produce a PTE small enough for us to include an extension that is not justified by the data. We explore the sensitivity of our results to this PTE threshold in detail in Section 6.2.

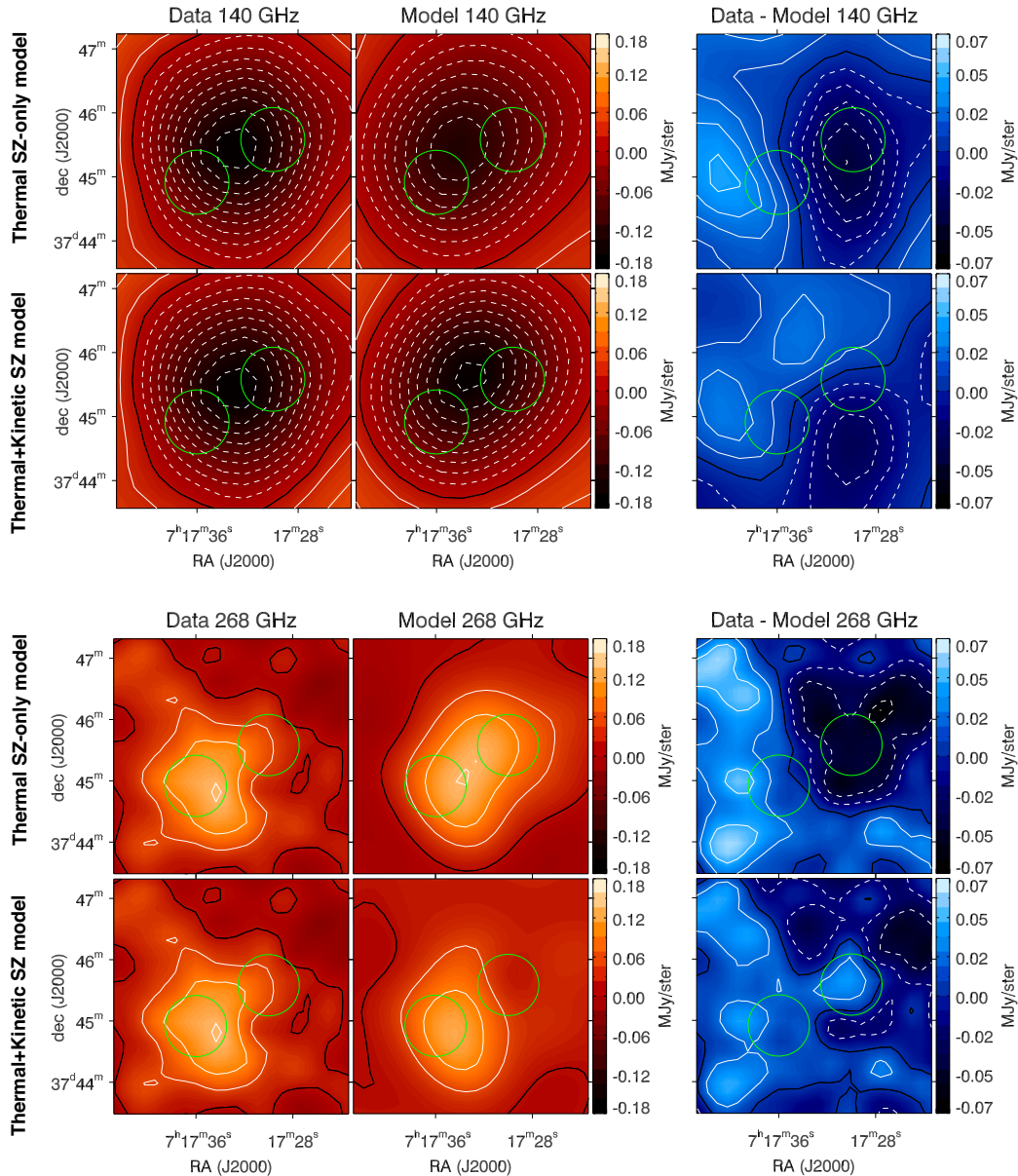


FIG. 3.— Bolocam thumbnails showing the processed data within the $4' \times 4'$ region we use to constrain our model of the SZ signal. From left to right the thumbnails show the Bolocam data, the best-fit model, and the difference between the data and the best-fit model (i.e., the residual map). The top block shows the 140 GHz data convolved with a $60''$ FWHM Gaussian, and the bottom block shows the 268 GHz data convolved with a $30''$ FWHM Gaussian. In the left plots, the contours are spaced by $S/N = 2$, with solid representing positive S/N , black representing 0, and dashed representing negative S/N . In the right plots the contours are spaced by $S/N = 1$, and the color stretch is reduced by a factor of 2.5 to better highlight the residuals between the data and the model. For each wavelength, the top row assumes a model composed of only the pseudo Compton- y map with a single normalization (a purely thermal SZ signal). This model is not a good fit to the data, and there is a clear dipole residual from ESE to WNW, at a significance of $\simeq 5\sigma$ at 140 GHz and $\simeq 3\sigma$ at 268 GHz. The bottom row for each wavelength assumes our nominal model of the pseudo Compton- y map with a single normalization plus an SZ template centered on sub-cluster B with different normalizations at 140 and 268 GHz (a thermal plus kinetic SZ signal). This model does provide a good fit to the data, and the residual maps are consistent with noise. The green circles are centered on sub-cluster C (lower left) and sub-cluster B (upper right), with diameters of $60''$.

four sub-clusters according to the positions given by Ma et al. (2009), allowing for different normalizations of the template at 140 and 268 GHz. We construct the SZ template according to the average profile constrained by Bolocam for a sample of 45 clusters (Sayers et al. 2013a), fixing the scale radius according to the estimated mass of each sub-cluster, which we obtain by using the ratios of sub-cluster masses determined by Limousin et al. (2012), in combination with the whole-cluster value of M_{500} de-

termined by Mantz et al. (2010). We note that this template represents a more physically motivated model than the Gaussian profile assumed by M12. We perform four separate fits, in each case fitting a single normalization to the pseudo Compton- y map (i.e., assuming that the pseudo Compton- y map contains only thermal SZ signal), along with separate normalizations at 140 and 268 GHz for an SZ template centered on one of the four sub-clusters (i.e., allowing the SZ template for that sub-

cluster to be free to include any arbitrary mixture of thermal and kinetic SZ signal). We find values of $\Delta\chi^2$ equal to 48.3, 108.1, 9.5, and 26.3 when the model contains an additional SZ template coincident with sub-clusters A, B, C, and D, respectively. These values of $\Delta\chi^2$ correspond to F-test PTEs of 0.001, 4×10^{-7} , 0.213, and 0.026. We note that the second value is extrapolated, due to the fact that we only have 1000 realizations of $\Delta\chi^2$.

As another possible extension to the baseline model of a pseudo Compton- y map with a single normalization in both Bolocam bands, we also explore the option of allowing for different normalizations of the pseudo Compton- y map at 140 and 268 GHz. Physically, this would represent a single bulk velocity for the entire cluster, with the cluster being isothermal so that the kinetic SZ signal has a spatial profile identical to the spatial profile of the thermal SZ signal. This fit results in a value of $\Delta\chi^2 = 52.1$, which corresponds to a simulated F-test PTE of 3×10^{-4} , where we have again used an extrapolation due to our finite number of realizations. Therefore, according to our F-test decision tree, we assume a new baseline model consisting of the pseudo Compton- y with a single normalization, along with a SZ template centered on sub-cluster B, as this is the model extension with the smallest simulated F-test PTE.

To fully characterize the fit of this new baseline model, we insert the best-fit model into each of our 1000 noise realizations, and then fit the same model to each of these realizations. The best-fit model has an overall $\chi^2 = 745.3$ for 715 degrees of freedom, which corresponds to a PTE of 0.29 based on the fits to the noise realizations, indicating that it provides an adequate description of our Bolocam SZ data.

Using this new baseline model, we again follow the F-test decision tree to determine whether the data still require an additional model extension. We perform three new fits that introduce an additional SZ component at A, C, and D to our baseline model. For these three fits, the value of $\Delta\chi^2$ is 23.9, 8.4, and 21.1, which corresponds to a simulated F-test PTE of 0.033, 0.260, and 0.046. As before, we also perform a fit allowing the normalization of the pseudo Compton- y map to be different at 140 and 268 GHz, and we find a $\Delta\chi^2 = 0.1$, with an associated simulated F-test PTE of 0.963. All of these fits have PTEs larger than 0.02, and we therefore conclude that none of these additional degrees of freedom are required to describe our data. Consequently, our baseline model of the SZ signal includes a pseudo Compton- y map with a single normalization, along with an SZ template centered on sub-cluster B with separate normalizations at 140 and 268 GHz (see Figure 3).

The data's strong lack of a preference for separate normalizations of the pseudo Compton- y map at 140 and 268 GHz justifies our choice of that model to describe the thermal component of the SZ signal. Furthermore, the best-fit normalization of the pseudo Compton- y map is 1.08 ± 0.11 . The pseudo Compton- y map was normalized based on the integrated SZ signal measured at 31 GHz by the SZA as reported in M12. Compared to the Bolocam observing bands, the kinetic SZ signal is a factor of $\simeq 2$ dimmer compared to the thermal SZ signal in the SZA observing band. Therefore, the consistent normalizations of the pseudo Compton- y map found by Bolocam and SZA further indicate that it provides a

good description of the thermal SZ signal toward MACS J0717.5+3745. As an additional cross-check, we also refit the normalization of the pseudo Compton- y map using the Bolocam data, but excluding the data within a $1'$ diameter aperture centered on sub-cluster B. This fit, which did not include any additional SZ components, results in a best-fit normalization of 1.13 ± 0.08 for the pseudo Compton- y map. The fit quality is good, with a PTE of 0.38, indicating that, outside sub-cluster B, the M12 pseudo Compton- y map, which was normalized to SZA, describes the Bolocam data well. Although these results serve as additional evidence that our model choice is physically justified, we emphasize that our results described below do not strictly depend on the pseudo Compton- y map being a good template for the thermal SZ signal, only that our model is physically motivated and provides an adequate description of the data.

6. MEASUREMENT OF THE SZ SPECTRUM TOWARD SUB-CLUSTER B

6.1. Two-Band SZ Photometry

Based on the requirement of an additional model component centered on sub-cluster B to describe our data, we compute the SZ brightness at both 140 and 268 GHz toward that sub-cluster. In order to eliminate as much contamination from other regions of the cluster as possible, we use a circular aperture with a diameter of $1'$, which is slightly larger than the PSF FWHM at 140 GHz. We first compute the average surface brightnesses within this aperture using the best-fit model from Section 5, convolved with the Bolocam PSF to accurately represent the resolution of the measurement. To include all of the subtle effects of the noise, such as the correlations between pixels due to residual atmospheric noise and primary CMB fluctuations, we also compute the average surface brightness within the same aperture using the model fits to the 1000 noise realizations. Kolmogorov-Smirnov (KS) tests against Gaussians on the distributions of 1000 values at 140 and 268 GHz yield PTEs of 0.19 and 0.93, respectively, and therefore indicate that our noise is Gaussian within our ability to measure it. Using these model fits, we estimate the surface brightness of sub-cluster B to be -0.344 ± 0.028 MJy sr $^{-1}$ at 140 GHz and 0.052 ± 0.029 MJy sr $^{-1}$ at 268 GHz, where the errors represent only measurement uncertainties.

In addition to the best-fit model, we also compute the surface brightness toward sub-cluster B by directly integrating our deconvolved images, which are shown in Figure 4. As described in Section 4.1, the deconvolved images have no sensitivity to the DC signal level. As a result, we determine the DC signal level of the deconvolved images using the best-fit model. Specifically, we add a signal offset to the deconvolved images so that the average signal level within the $4' \times 4'$ region we use to constrain the model is equal to the average signal level of the best-fit model within the same region. We exclude the $1'$ diameter aperture centered on sub-cluster B in this calculation to avoid any potential bias in the surface brightness we derive within that aperture. This direct integration yields average surface brightnesses of -0.341 ± 0.027 MJy sr $^{-1}$ and 0.095 ± 0.049 MJy sr $^{-1}$, respectively, where we have again estimated the uncertainties using the 1000 noise realizations. As with the model derived results, we used a KS test to determine if the

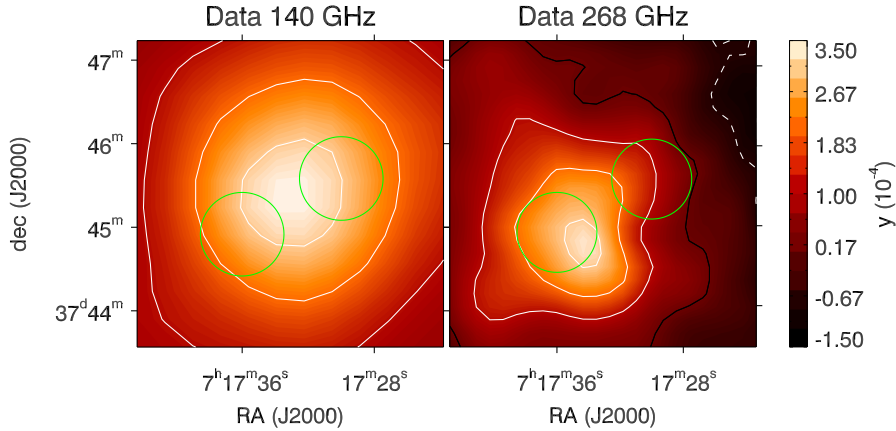


FIG. 4.— Thumbnails of the deconvolved Bolocam images at 140 and 268 GHz. We have scaled both images to units of Compton- y , including positionally dependent relativistic corrections based on the X-ray-determined temperature map. The relativistic corrections generally range from 8 – 15% at 140 GHz and from 20 – 40% at 268 GHz. The 140 GHz image is smoothed with a $60''$ Gaussian, and the 268 GHz image is smoothed with a $30''$ Gaussian. The contours are spaced by 1×10^{-4} , with solid showing positive y and dashed showing negative y . The green circles show the $1'$ diameter apertures centered on sub-cluster C (lower left) and sub-cluster B (upper right). The total Compton- y signal toward sub-cluster C is nearly identical at the two wavelengths, while there is a clear difference toward sub-cluster B.

distribution of 1000 values is consistent with Gaussian, and we find PTEs of 0.75 and 0.57 at 140 and 268 GHz, respectively. We note that these surface brightness values are consistent with those derived from the best-fit model, although there is significantly more measurement uncertainty on the 268 GHz value. This additional uncertainty is a result of the significant large-angular-scale atmospheric noise in those data, which is amplified by the deconvolution of the signal transfer function.

6.2. Systematic Uncertainties

First, we note that our flux calibration is accurate to 5% at 140 GHz, and to 10% at 268 GHz (Sayers et al. 2012). We have included these uncertainties in our systematic error budget.

To estimate the systematic errors due to the model-dependence of our results, we repeat our analysis of computing model-based and directly integrated surface brightnesses toward sub-cluster B at both 140 and 268 GHz using a range of different models, with a summary of the results in Table 1. First, we replace the baseline pseudo Compton- y map we use in our model with a set of 20 realizations of the pseudo Compton- y map that we generate according to the X-ray measurement uncertainties on the mean T_e for each *contbin* region (see Section 4.2). Next, we constrain our baseline model using $3' \times 3'$ and $5' \times 5'$ regions of the Bolocam images instead of the nominal $4' \times 4'$ region we use in Section 5. In addition, we consider an SZ model that does not include the pseudo Compton- y map, and instead only includes SZ templates centered on the sub-clusters. We repeat the F-test decision tree described in Section 5 to determine which of the sub-clusters require an SZ template for this model. We find that, without the pseudo Compton- y map, the data require SZ templates centered on sub-clusters B, C, and D. This fit produces a PTE of 0.64, indicating that the data are adequately described by this model.¹⁶ Furthermore, we re-ran the F-test decision tree with the PTE threshold increased by a factor of two to

¹⁶ The adequacy of this somewhat simple and ad-hoc model in describing our data is likely due to Bolocam’s coarse angular resolution, which largely blurs any sub-structures not well described

0.04. With this new threshold, the model consists of the pseudo Compton- y map with a single normalization, along with SZ templates centered on sub-clusters A and B (i.e., relative to the baseline model, an additional SZ template is required for sub-cluster A). Finally, we determine the effects of varying the scale radius of the profile used as a template of the SZ signal toward sub-cluster B. We vary the scale radius over a range of 0.67 – 1.5 times its nominal value, which corresponds to a scaling of the assumed mass of sub-cluster B by a factor of 0.3 – 3.4.

Considering this broad range of possible models that we could have chosen to describe our data, we find that the model-derived surface brightness of sub-cluster B never changes by more than 1.0 times the measurement uncertainties given in Section 6.1. For the surface brightness values obtained from direct integration of the deconvolved images, we find that the change is never larger than 0.6 times the uncertainties given in Section 6.1. As expected, the model-derived surface brightnesses have a stronger model dependence compared to the directly integrated surface brightnesses, although the latter still have a noticeable model-dependence due to the method by which we constrain the DC signal level of the deconvolved image. Based on these results, we conservatively include an additional systematic uncertainty of 1.0 times the measurement uncertainty for the model-derived surface brightnesses, and 0.6 times the measurement uncertainty for the directly integrated surface brightnesses. A full summary of our best-fit surface brightnesses, along with the full error budget on these values, is given in Table 2.

In addition to exploring how our choice of model affects our results, we also examine the effects of varying the aperture we use to compute the average surface brightness toward sub-cluster B. First, we examine three possible choices for the location of sub-cluster B: 1) the location given by Ma et al. (2009) based on the distribution of galaxies ($7:17:30.0$, $+37:45:35$), 2) the location given by

by the smooth SZ templates. However, we note that this model requires twice as many free parameters as our baseline model in order to obtain an adequate fit according to our F-test decision tree.

TABLE 1
 VARIATIONS IN SUB-CLUSTER B'S SURFACE BRIGHTNESS DUE TO
 POSSIBLE CHANGES IN OUR ANALYSIS METHOD

Model-Derived		Direct Integration	
140 GHz	268 GHz	140 GHz	268 GHz
MJy sr ⁻¹	MJy sr ⁻¹	MJy sr ⁻¹	MJy sr ⁻¹
Nominal Values from Baseline Model			
-0.344 ± 0.028	0.052 ± 0.029	-0.341 ± 0.027	0.095 ± 0.049
Variations due to Model Choice			
vary pseudo Compton- y within X-ray uncertainties			
± 0.012 ($\pm 0.4\sigma$)	± 0.009 ($\pm 0.3\sigma$)	± 0.006 ($\pm 0.2\sigma$)	± 0.004 ($\pm 0.1\sigma$)
vary region used for fit from 3' to 5'			
≤ 0.003 ($\leq 0.1\sigma$)	≤ 0.019 ($\leq 0.7\sigma$)	≤ 0.003 ($\leq 0.1\sigma$)	≤ 0.024 ($\leq 0.5\sigma$)
model with no pseudo Compton- y ; templates at B, C, and D			
0.028 (1.0 σ)	0.026 (0.9 σ)	0.016 (0.6 σ)	0.015 (0.3 σ)
F-test decision tree with PTE threshold equal to 0.04			
0.007 (0.3 σ)	0.017 (0.6 σ)	0.001 (0.0 σ)	0.026 (0.5 σ)
vary scale radius of B template by 0.67 to 1.5			
≤ 0.017 ($\leq 0.6\sigma$)	≤ 0.026 ($\leq 0.9\sigma$)	≤ 0.017 ($\leq 0.6\sigma$)	≤ 0.022 ($\leq 0.4\sigma$)
Variations due to Aperture Choice			
aperture centered on Limousin et al. (2012) coords			
0.018 (0.6 σ)	0.019 (0.7 σ)	0.009 (0.3 σ)	0.003 (0.1 σ)
aperture centered on X-ray centroid			
0.019 (0.7 σ)	0.034 (1.2 σ)	0.010 (0.4 σ)	0.048 (1.0 σ)
vary aperture diameter from 0.67' to 1.5'			
≤ 0.029 ($\leq 1.0\sigma$)	≤ 0.013 ($\leq 0.4\sigma$)	≤ 0.024 ($\leq 0.9\sigma$)	≤ 0.011 ($\leq 0.2\sigma$)

NOTE. — Top block: best-fit surface brightnesses from the baseline model described in Section 5, and associated 1σ uncertainties due to measurement noise only. Next block: variations in the surface brightness of sub-cluster B based on our choice of model. We consider five different model fits to describe the SZ data. These models are explained in detail in the text, and we refer the reader there for more details. From left to right, the columns give the change in surface brightness at 140 and 268 GHz for the model-derived and direct integration surface brightnesses. The top rows give these values in MJy sr⁻¹, and the bottom rows give these values relative to the measurement uncertainties in the top block. When noise variations to the models are considered, these values indicate the 1σ range with a \pm symbol, when a range of model inputs are considered, these values show the magnitude of the maximum change with a \leq symbol, and when a single alternative model is considered these values show the magnitude of the change with no symbol. Based on these results, we add a systematic uncertainty equal to 1.0 times the measurement uncertainty for the model-derived values and equal to 0.6 times the measurement uncertainty for the direct integration values. Bottom block: variations in the surface brightness of sub-cluster B for different choices of aperture. From top to bottom, the rows show the change relative to our nominal 1' diameter aperture centered on the Ma et al. (2009) coordinates for 1) an aperture centered on the Limousin et al. (2012) coordinates, 2) an aperture centered on the X-ray centroid, and 3) varying the aperture diameter between 0.67' and 1.5' for the aperture centered on the Ma et al. (2009) coordinates. All of these differences are consistent with the expected measurement noise fluctuations for the different aperture choices.

Limousin et al. (2012) based on the matter distribution (7:17:30.2, +37:45:15), and 3) the location of the X-ray brightness centroid (7:17:31.4, +37:45:29). Our nominal analysis uses the Ma et al. (2009) coordinates, and we give the changes in surface brightness when we use the other two possible apertures in Table 1. Compared to the measurement uncertainties given in Section 6.1, the surface brightnesses we measure in these new apertures differ by less than $\leq 1.2\sigma$ with a median of $\simeq 0.7\sigma$. The three sets of coordinates are separated from each other by $\simeq 20''$, which is a significant fraction of the aperture radius of $30''$, and means that less than 50% of the area enclosed by one aperture is also enclosed by another aperture. Consequently, completely uncorrelated measurement noise between any given pair of apertures will produce surface brightnesses that differ by $\simeq 1\sigma$. Therefore, the differences in surface brightness that we measure between these aperture locations are consistent with the expectation due to noise fluctuations.

We also examine the effects of varying the diameter of the aperture from 0.67' to 1.5' (compared to the nominal diameter of 1'), and again find results that are consistent within 1σ . As with the different aperture locations, this is consistent with the variations that we expect due to uncorrelated measurement noise between the aperture choices, and indicates that variations in the location, or diameter, of the aperture we use to measure the SZ surface brightness result in differences consistent with measurement noise. We therefore conclude that our results are not sensitive to the exact choice of aperture, and we do not include any additional systematic error in our overall noise budget. We note that in all cases the apertures are comparable in size to the Bolocam PSF, and there is consequently some signal leakage from outside to inside the apertures and vice versa. Furthermore, the separation between the apertures centered on sub-clusters B and C is also comparable to the size of the Bolocam PSF, and so there is some signal leakage between apertures. Although we are not able to account for this signal leakage in our analysis, the consistency of our results using various aperture positions and diameters indicates that the leakage is below our measurement uncertainties.

6.3. Comparison to Previous Results

We note that the 140 GHz surface brightnesses we find for sub-cluster B are slightly different compared to the values reported in M12, although identical Bolocam data is used for both analyses. Our model-derived surface brightness of -0.344 ± 0.028 MJy sr⁻¹ is more than 1σ lower than the M12 value of -0.293 ± 0.030 MJy sr⁻¹.¹⁷ More than half of this difference is due to a minor error in the analysis presented in M12. The total flux densities given in Table 3 of M12 were mistakenly computed from the average surface brightness within a 1.5' aperture, rather than the 1' aperture claimed in the text of M12 and also used in our present analysis. The remaining difference between our current surface brightness values and the ones presented in M12 is due to minor changes in our assumed model of the SZ signal. First, M12 constrained

¹⁷ Table 3 of M12 lists a total flux density of -19.5 ± 2.0 mJy, which corresponds to a surface brightness of -0.293 ± 0.030 MJy sr⁻¹.

TABLE 2
SZ SURFACE BRIGHTNESS

Frequency GHz	Best Fit MJy sr ⁻¹	Measurement Err. MJy sr ⁻¹	Flux Err. MJy sr ⁻¹	Modeling Err. MJy sr ⁻¹	Total Err. MJy sr ⁻¹
Sub-Cluster B					
Model Fits					
140	-0.344	0.028	0.017	0.028	0.043
268	0.052	0.029	0.005	0.029	0.041
Direct Integration					
140	-0.341	0.027	0.017	0.016	0.036
268	0.095	0.049	0.010	0.029	0.058
Sub-Cluster C					
Model Fits					
140	-0.262	0.026	0.013	0.028	0.040
268	0.217	0.039	0.022	0.029	0.053
Direct Integration					
140	-0.270	0.026	0.014	0.016	0.034
268	0.220	0.059	0.022	0.029	0.069

NOTE. — The average surface brightness within a 1' diameter aperture centered on sub-clusters B and C. From left to right the columns give the observing frequency, the best-fit average surface brightness, the measurement uncertainty on this value, the uncertainty on this value due to flux calibration, the uncertainty on this value due to the range of models we could have chosen to describe the data, and the total combined uncertainty which is the quadrature sum of the previous three columns. For each sub-cluster, the top rows give the values we derive from the best-fit model of the SZ signal, and the bottom rows give values we derive from direct integration of the deconvolved images.

the normalization of the pseudo Compton- y map separately at 140 and 268 GHz, compared to the joint constraint we use in our present analysis. In addition, M12 assumed that the SZ template centered on sub-cluster B had a Gaussian profile, compared to the more physically motivated profile we use in this analysis, with a shape described by the best-fit profile to a sample of 45 clusters observed with Bolocam (Sayers et al. 2013a).

Furthermore, we note that, in our current analysis, the model-derived surface brightness agrees quite well with the surface brightness we obtain from a direct integration of the deconvolved image. This result is in contrast to the measurements presented in M12, where the two values differed by slightly more than 1σ . This change is due to differences in how the DC signal offset of the deconvolved images is computed. M12 computed the DC signal offset based on a fit of the average profile determined by Arnaud et al. (2010) to the full 140 GHz Bolocam dataset. Although the fit quality of this single profile is not particularly poor, with a PTE of 0.07, the adequacy of using a single profile to describe a complex merging system like MACS J0717.5+3745 is questionable. Therefore, as described above, for this analysis we choose to constrain the DC signal offset of the 140 GHz deconvolved image using our nominal model of the SZ signal (a pseudo Compton- y map with an additional SZ component centered on sub-cluster B). Not surprisingly, this change in our estimate of the DC signal level results in a better agreement between the model-derived and directly integrated surface brightnesses.

7. MEASUREMENT OF THE SZ SPECTRUM TOWARD SUB-CLUSTER C

M12 computed the SZ surface brightness toward both sub-cluster B and sub-cluster C. The latter measurement was motivated primarily by the fact that Ma et al. (2009) identified sub-cluster C as the most massive component of MACS J0717.5+3745, along with the fact that sub-cluster C is coincident with the highest surface brightness in the 268 GHz Bolocam image. Therefore, although our F-test decision tree indicates that our data do not require a component in addition to the thermal SZ template toward sub-cluster C, we again measure its SZ surface brightness. For these measurements we add an SZ template centered on sub-cluster C to our model, to ensure that the model has enough freedom to describe any possible deviations from a purely thermal SZ spectrum. We again estimate the SZ surface brightness using a 1' diameter aperture centered on the coordinates from Ma et al. (2009), with the results given in Table 2. As with sub-cluster B, we estimate the uncertainties on these surface brightnesses using our 1000 noise realizations, and we again find that the distribution of values is consistent with Gaussian noise. In addition, we estimate the systematic uncertainty due to our choice of model using the same formalism described for sub-cluster B in Section 6.2. We find systematic errors consistent with those that we find for sub-cluster B, and we therefore adopt identical values for sub-cluster C. Finally, we note that the 140 GHz brightness values differ from those derived in M12 by roughly the same amounts as for sub-cluster B, with the differences due to the same reasons described in detail in Section 6.3.

We do not attempt to constrain the SZ brightness toward either sub-cluster A or sub-cluster D. We do not consider sub-cluster A due to the fact that it is not strongly detected in either Bolocam dataset. We do

not consider sub-cluster D due to the fact that it is not separately resolved from sub-cluster C due to Bolocam’s coarse angular resolution, and therefore any estimate of sub-cluster D’s SZ brightness would be highly correlated with our estimate of sub-cluster C’s SZ brightness.

8. PECULIAR VELOCITY CONSTRAINTS

Using our two-band measurements of the SZ surface brightness toward sub-clusters B and C, we are able to place constraints on the properties of the ICM of each sub-cluster. Based on the equations presented in Section 2, the total SZ brightness depends on four quantities related to the cluster ICM: $f(\nu, T_e)$, y , τ_e , and v_z . Our two-band SZ surface brightness measurements are insufficient to constrain all of these quantities, and so we therefore make the assumption that the ICM within each sub-cluster is isothermal and equal to the X-ray spectroscopic temperature determined within the same $1'$ diameter apertures that we use to measure the SZ surface brightness. As a result, $f(\nu, T_e)$ is fully constrained by the *Chandra*-and-*XMM*-measured T_e , and from Equations 4 and 2 we have $y = \tau_e k_B T_e m_e^{-1} c^{-2}$, meaning that y and τ_e are not independent. Therefore, we are left with two free parameters to constrain using the two-band Bolocam surface brightnesses, either τ_e and v_z or y and v_z (in practice we constrain Y_{int} and v_z , where $Y_{int} = y\Delta\Omega$, and $\Delta\Omega$ is equal to the solid angle of our $1'$ aperture). In all of the fits, we compute the band-averaged values of $f(\nu, T_e)$ for a given T_e using the full Bolocam bandpasses rather than a single effective band center.

Using our X-ray measured T_e , along with our SZ surface brightnesses, we then perform a grid search to constrain the values of v_z and Y_{int} for sub-clusters B and C. For these constraints, we use the best-fit SZ surface brightness values from Table 2, along with the total uncertainties in the far-right column of that table. Therefore, we fully include not only measurement uncertainties, but also flux calibration uncertainties, and possible systematic uncertainties due to our choice of model to describe the SZ signal. Because the noise in our SZ surface brightness measurements is indistinguishable from Gaussian, we compute likelihoods based on a Gaussian distribution. When fitting the SZ spectra, we marginalize over the range of T_e values allowed by the X-ray data, relying on the χ^2 statistic to give a likelihood for each temperature in the range 2 – 40 keV. A summary of our results for both sub-clusters is given in Table 3 and Figures 5 and 6, and we highlight some of these results below.

For sub-cluster B we find a best-fit $v_z = +3450$ km s $^{-1}$ using the SZ surface brightnesses we determine from the model fit to our data and a best-fit $v_z = +2550$ km s $^{-1}$ using the SZ surface brightnesses we determine from direct integration of our deconvolved images. Both of these values are consistent with the value of $+3238$ km s $^{-1}$ determined by Ma et al. (2009) based on optical spectroscopy under the assumption that the peculiar velocity of the entire cluster is 0 along the line-of-sight (see Figure 5). The 1σ uncertainties about these best-fit velocities are similar for both the model-derived and direct integration results, and are $\lesssim 1000$ km s $^{-1}$. We also compute the probability of $v_z \geq 0$, and we obtain values of $(1 - \text{Prob}[v_z \geq 0]) = 1.3 \times 10^{-5}$ and 2.2×10^{-3} for the model-derived and direct integration SZ surface brightnesses, respectively (see the bottom panels of Figure 5).

For a Gaussian distribution, these one-sided probabilities correspond to a difference from $v_z = 0$ of 4.2σ and 2.9σ , respectively. For sub-cluster C we find a best-fit v_z of $\simeq -500$ km s $^{-1}$ from both the model fit and direct integration of the deconvolved image, which is fully consistent with both the value of -733 km s $^{-1}$ determined by Ma et al. (2009) and with zero velocity. We note that the uncertainties on the value of v_z for sub-cluster C are $\simeq 50\%$ larger compared to sub-cluster B. This increase is due entirely to the higher temperature of sub-cluster C. This higher temperature produces a smaller value of τ_e for a fixed value of Y_{int} and therefore a correspondingly lower kinetic SZ signal for a fixed value of v_z .

We note that the difference between our best-fit v_z and the best fit v_z from Ma et al. (2009) is quite small for both sub-clusters (0.23σ and 0.13σ for the model-derived results for sub-clusters B and C, and 0.64σ and 0.14σ for the direct-integration results for sub-clusters B and C). The random probability of obtaining such results from two independent measurements of two independent parameters is 2% for our model-derived results and 6% for our direct-integration results. These probabilities are small, but they are not small enough to cause significant concern. In addition, our intentionally conservative estimates of the uncertainties due to our choice of SZ model have likely resulted in over-estimated errors on the SZ brightness, thus rendering the good agreement between our results and those of Ma et al. (2009) more likely.

9. DISCUSSION

9.1. Differences Compared to the Results in M12

Compared to the results presented in M12, our best-fit values of v_z for sub-cluster B are somewhat lower ($+3450$ km s $^{-1}$ and $+2550$ km s $^{-1}$ compared to $+4640$ km s $^{-1}$ and $+3600$ km s $^{-1}$ for the model-derived and direct integration surface brightnesses, respectively). This is mainly due to an increase in the best-fit surface brightness at 268 GHz as a result of the additional data we use in our present analysis. In contrast, our best-fit values of v_z for sub-cluster C are smaller in magnitude compared to M12 (-550 km s $^{-1}$ and -500 km s $^{-1}$ compared to -3720 km s $^{-1}$ and -4120 km s $^{-1}$ for the model-derived and direct integration surface brightnesses, respectively). These differences are again driven by the additional 268 GHz data we use in our current analysis, which indicates that sub-cluster C is dimmer compared to the analysis of M12. However, we emphasize that all of our measured values of v_z are consistent to within 1σ of the values presented in M12, and there is no tension between the two results.

Our uncertainties on the value of v_z for sub-cluster B are a factor of $\simeq 3$ smaller than the uncertainties reported in M12. This improvement is almost entirely due to the significant amount of additional 268 GHz data we use in this analysis and the corresponding factor of $\simeq 2.5$ decrease in the uncertainties on the 268 GHz surface brightness. A small additional improvement is driven by the lower value of T_e found in our present analysis, which for a fixed Y_{int} corresponds to a larger τ_e and therefore a larger kinetic SZ signal for a fixed v_z . In contrast, our uncertainties on v_z for sub-cluster C have only decreased by a factor of $\simeq 2$ compared to M12 even though there is a similar reduction in the 268 GHz measurement un-

TABLE 3
PECULIAR VELOCITY CONSTRAINTS

	T_e keV	optical km s ⁻¹	SZ model fit km s ⁻¹	SZ direct integration km s ⁻¹
sub-cluster B	$11.4^{+0.5}_{-0.5}$	$+3238^{+252}_{-242}$	$+3450^{+900}_{-900}$ ($1 - \text{Prob}[v_z \geq 0] = 1.3 \times 10^{-5}$)	$+2550^{+1050}_{-1050}$ ($1 - \text{Prob}[v_z \geq 0] = 2.2 \times 10^{-3}$)
sub-cluster C	$19.9^{+1.5}_{-1.4}$	-733^{+486}_{-478}	-550^{+1350}_{-1400} ($1 - \text{Prob}[v_z \leq 0] = 3.7 \times 10^{-1}$)	-500^{+1600}_{-1550} ($1 - \text{Prob}[v_z \leq 0] = 4.3 \times 10^{-1}$)

NOTE. — Line-of-sight velocity constraints from our analysis. From left to right the columns give the the X-ray-derived temperature from *Chandra* and *XMM*, the line-of-sight velocity derived by Ma et al. (2009) based on optical spectroscopy, and the line-of-sight velocity from our kinetic SZ constraints using the best-fit model and a direct integration of the deconvolved image. The top row shows the constraints for sub-cluster B, and the bottom row shows the constraints for sub-cluster C. For the fits we have used the best-fit SZ brightnesses given in Table 2, with the total uncertainties listed in the far-right column of that table. Next to the kinetic SZ velocity constraints, we give the probability that the line-of-sight velocity is greater than 0 for sub-cluster B, and the probability that the line-of-sight velocity is less than 0 for sub-cluster C.

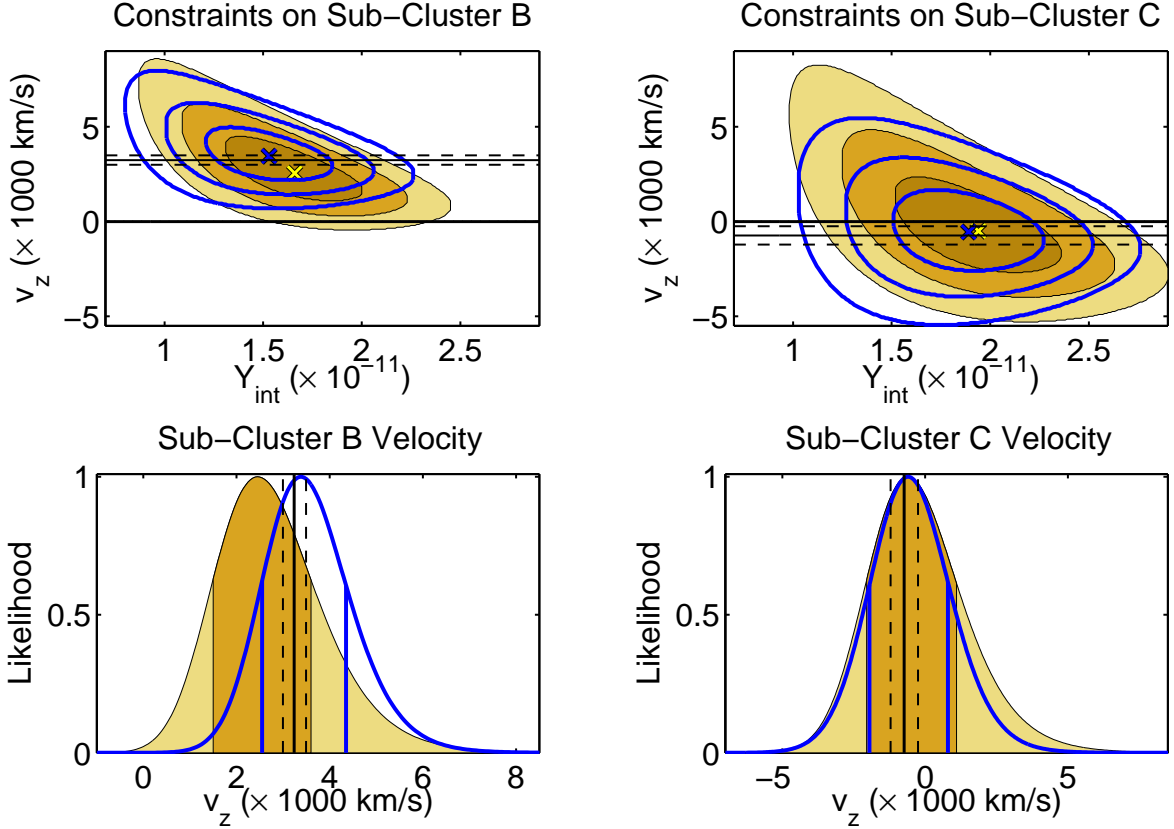


FIG. 5.— Our SZ-derived constraints on the ICM toward sub-cluster B (left) and sub-cluster C (right). The top row shows two-dimensional confidence regions for the values of Y_{int} and v_z , with contours drawn at 1σ , 2σ , and 3σ for a two-parameter likelihood (e.g., 1σ corresponds to a $\Delta\chi^2 = 2.30$). The bottom row shows marginalized one-dimensional likelihoods for v_z , with vertical lines drawn at $\pm 1\sigma$ (corresponding to $\Delta\chi^2 = 1$). In all cases blue corresponds to the constraints from the model-derived SZ surface brightnesses, and yellow corresponds to the constraints from the SZ surface brightnesses we derive from direct integration of the deconvolved images. The solid black line represents the best-fit velocity derived by Ma et al. (2009) based on optical spectroscopy, and the dashed lines show the corresponding 1σ confidence region around their best-fit.

certainties. This difference relative to sub-cluster B is driven by our best-fit value of v_z , which is significantly larger (less negative) than the results in M12. As a result, the best-fit value of Y_{int} is smaller, and therefore the best-fit value of τ_e is smaller. Consequently, for a given change in v_z , the corresponding change in the kSZ surface brightness is also smaller, resulting in less constraining power on the value of v_z .

In contrast to the analysis presented in M12, note that we include additional systematic uncertainties in our derived SZ surface brightnesses due to differences based on

the range of models we could have chosen to describe the SZ signal. These systematic uncertainties increase the total error estimate on the model-derived and directly integrated SZ surface brightnesses by $\simeq 40\%$ and $\simeq 20\%$, respectively. We perform fits of v_z without including this additional systematic error, and verify that the fractional improvement in our constraints matches these values. Therefore, the model-dependence of our SZ data results in a non-negligible degradation of our constraining power on v_z .

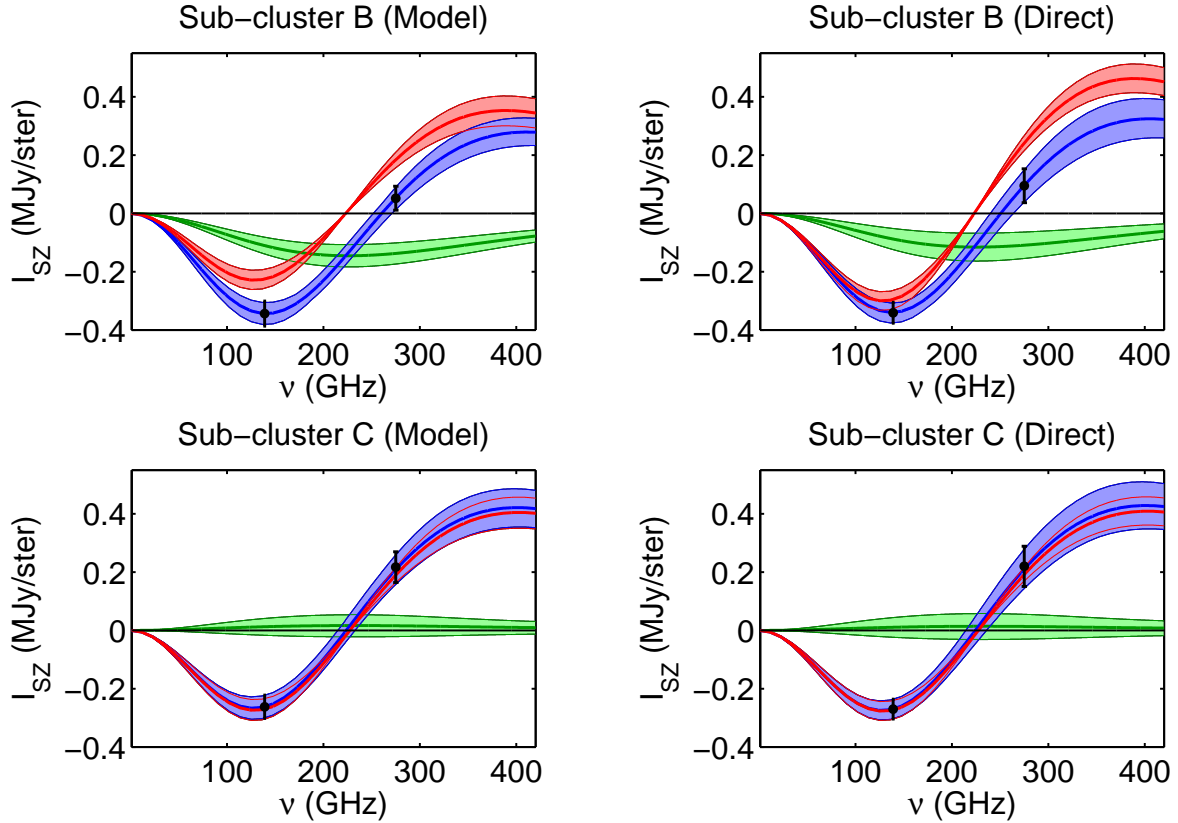


FIG. 6.— Our best-fit SZ spectra. The top row shows the fits to sub-cluster B, and the bottom row shows the fits to sub-cluster C. The left column shows the SZ surface brightnesses we determine from the model fit, and the right column shows the SZ surface brightnesses we determine via direct integration of the deconvolved images. The best-fit thermal-SZ-only spectrum is shown in red, the best-fit kinetic SZ spectrum is shown in green, and the best-fit thermal plus kinetic SZ spectrum is shown in blue, with the widths showing the 1σ confidence region of the fits. We include relativistic corrections in all of the spectra.

9.2. Limitations to Our Kinetic SZ Constraints

Given the range of multi-wavelength data that we use to place constraints on v_z , we also estimate how each of these datasets contribute to our overall uncertainties. First, as noted in Section 4.3, previous results have indicated that there is a systematic difference in temperatures derived from *Chandra* and *XMM*, and the temperatures we measure are in general agreement with this systematic difference. At this point, the cause of this difference has not been conclusively demonstrated. Due to this lack of a conclusive understanding of the difference, combined with the fact that the difference between the X-ray temperatures we derive from the two observatories is of modest statistical significance, we choose to constrain the electron temperatures via the joint likelihood from the *Chandra* and *XMM* data. If we instead adopt the *XMM*-only values of T_e , then we find best-fit values of v_z equal to $+3300 \text{ km s}^{-1}$ and $+2450 \text{ km s}^{-1}$ for the model fit and direct integration of sub-cluster B and -450 km s^{-1} and -400 km s^{-1} for the model fit and direct integration of sub-cluster C. If we instead adopt the *Chandra*-only values of T_e , then we find best-fit values v_z equal to $+4000 \text{ km s}^{-1}$ and $+2900 \text{ km s}^{-1}$ for the model fit and direct integration of sub-cluster B and -550 km s^{-1} and -450 km s^{-1} for the model fit and direct integration of sub-cluster C. For sub-cluster B, the *Chandra*-only temperatures yield line-of-sight velocities that differ by $\simeq 0.5\sigma$, but all of the other values are statistically indistinguishable from our results in Table 3. Therefore,

we conclude that X-ray calibration uncertainties do not strongly affect our constraints on v_z . We further note that the significance of our kinetic SZ measurement from $v_z = 0$ is nearly independent of the exact value of T_e and the slight differences in v_z for the different temperatures are due to the inverse relationship between T_e and τ_e for a fixed y , coupled with the inverse relationship between v_z and τ_e for a fixed kinetic SZ surface brightness.

To assess the impact of the X-ray uncertainties on T_e , we also rerun all of our fits with vanishing uncertainties on the X-ray derived T_e . Even in the case of sub-cluster C, when using the *Chandra*-only measurement with uncertainties of $T_e \begin{smallmatrix} +7.8 \\ -3.8 \end{smallmatrix} \text{ keV}$, the derived uncertainties on v_z increase by only $\simeq 10\%$ when using the measured uncertainties instead of assuming that the uncertainty on T_e is equal to 0. Therefore, the X-ray uncertainties are not significant in our overall error budget on v_z .

To determine the effect of the CIB on our measurement of v_z , we also compute the SZ brightness under the assumption that the CIB is completely and noiselessly subtracted from the data. Specifically, compared to our default noise realizations, we remove the noise from the undetected CIB, along with our uncertainties on the subtracted CIB (see the Appendix). This results in a negligible change in the 140 GHz surface brightness uncertainties, and a $\simeq 10\text{--}20\%$ reduction in the 268 GHz surface brightness uncertainties. There is a corresponding $\simeq 10\text{--}20\%$ reduction in our derived uncertainties on v_z . In addition, we estimate the potential bias that

would result from not subtracting any of the Bolocam or SPIRE-detected galaxies from our 268 GHz data. We find that our best-fit 268 GHz surface brightness values change by $\simeq 10\%$, indicating that the bright sources in the CIB produce a non-negligible bias in the SZ surface brightnesses we measure. Therefore, at our sensitivities, the CIB has a noticeable effect on our kinetic SZ measurement, and is more significant than uncertainties on the X-ray-derived electron temperature.

We also perform fits under the assumption that primary CMB fluctuations are perfectly subtracted from our data by removing them from our noise realizations. This does not produce a noticeable change in the 268 GHz surface brightness constraints, but does improve the 140 GHz surface brightness constraints by $\simeq 5\%$, with a corresponding improvement in our derived constraints on v_z . Therefore, noise from primary CMB fluctuations has an effect on our kinetic SZ measurements that is smaller than, but comparable to, noise from CIB fluctuations. This mild sensitivity to primary CMB fluctuations is due to the relative shallowness of our 140 GHz data, which have an rms of $\simeq 30 \mu\text{K}_{\text{CMB-arcmin}}$ (see Table 1 of Sayers et al. 2013a).

Examining the error budget in Table 2, the dominant uncertainties are associated with SZ measurement noise and the exact choice of model used to describe the SZ data, although we note that uncertainties due to absolute flux calibration are only a factor of $\simeq 2$ smaller. As detailed in Section 4.1, a model is required to interpret our SZ data because the large-angular scale atmospheric noise necessitates high-pass filtering of the data, which removes signal on large angular scales. As a result, a spatial model of the SZ is the only way to recover this large-scale signal in order to obtain an absolute surface brightness. Therefore, this modeling uncertainty is a direct result of the measurement noise in the SZ data, and is not a fundamental limitation. Consequently, deeper SZ data would provide a significant improvement to our kinetic SZ measurement, although these deeper SZ data will require better absolute flux calibration, are likely to require an improved subtraction of the CIB (and possibly the primary CMB fluctuations), and may require an improved understanding of the X-ray temperature calibration or the line-of-sight temperature structure (e.g., Chluba et al. 2012; Prokhorov & Colafrancesco 2012).

9.3. Additional Potential Sources of Bias

Our analysis constrains the line-of-sight peculiar velocities of two of the sub-clusters of MACS J0717.5+3745 via a measurement of the SZ surface brightnesses within small apertures centered on these sub-clusters. Due to the complex dynamics in MACS J0717.5+3745, the SZ signal within these apertures may not be sourced by gas bound to a single sub-cluster with a single coherent bulk velocity. However, as described in Section 3, the X-ray data show that sub-cluster B does appear to have a relatively intact core region. Therefore, at least for sub-cluster B, the assumption of a single bound ICM appears to be justified. Sub-cluster C seems to be more disturbed, and this assumption may not be valid for that region.

In addition to possible merger-induced gas inhomogeneities, there are also likely to be line-of-sight projection effects that cause the SZ signal within a single aperture to be sourced by the ICMs of multiple sub-clusters.

In part to answer this question, Ruan et al. (2013) studied the SZ signal from a simulated triple-merger system in detail. Their simulated cluster is similar to MACS J0717.5+3745, and contains one sub-cluster with a velocity of 2500 km s^{-1} . They used kinetic SZ measurements at 90 and 268 GHz to constrain the line-of-sight velocities of sub-clusters within the merger and found best-fit velocities that are consistent with the true velocities of the sub-clusters to within $\simeq 10\%$. This is partly due to the fact that the SZ signal from the core of the sub-cluster of interest is significantly brighter than the SZ signal away from the core of other sub-clusters in projection. However, the merging sub-cluster also induces a small kinetic SZ signal in the ICMs of the other sub-clusters in projection with it, and this induced signal serves to bring the SZ-measured velocity into better agreement with the true velocity. These results indicate that at our current measurement precision, the bias in our measured velocities due to interactions and projection effects from other sub-clusters is likely to be statistically insignificant.

9.4. Cosmological Implications

Our kinetic SZ measurements are in good agreement with the spectroscopic measurements of Ma et al. (2009) and indicate that sub-cluster B is moving with a line-of-sight velocity of $\simeq 3000 \text{ km s}^{-1}$ compared to the center of mass of the system. Ma et al. (2009) note that this value is close to the maximum expected velocity due to infall from infinity. For example, if sub-cluster B starts from rest at infinity, and if the main cluster has a mass of $1.5 \times 10^{15} M_{\odot}$, then sub-cluster B would need to be within $\simeq 1.5 \text{ Mpc}$ of the main cluster to reach an infall velocity of 3000 km s^{-1} . This is in fairly good agreement with N-body simulations, which indicate that a relative velocity of $\simeq 3000 \text{ km s}^{-1}$ is possible for a MACS J0717.5+3745-like cluster within the framework of the standard cosmological model. For example, Lee & Komatsu (2010) showed that mergers with main cluster masses above $1 \times 10^{15} M_{\odot}$ at $z = 0.5$ have a non-negligible probability of producing velocities larger than 3000 km s^{-1} when the sub-cluster is within the virial radius of the main cluster. In addition, the cluster studied by Ruan et al. (2013, see Section 9.3) was selected from a cosmological simulation of a $400 h^{-1} \text{ Mpc}$ cube, and one of its sub-clusters has a line-of-sight velocity of 2500 km s^{-1} . Therefore, we conclude that while the velocity of sub-cluster B is large, it is not in any tension with the standard cosmological models.

10. SUMMARY

We detect an extended SZ signal toward MACS J0717.5+3745 at high significance in two observing bands with Bolocam (140 and 268 GHz). The 268 GHz data also contain significant emission from dusty star forming galaxies. We subtract all of the galaxies brighter than $\simeq 1 \text{ mJy}$ using a combination of *Herschel*-SPIRE and Bolocam data, although both this subtraction, and the un-subtracted population of dimmer galaxies, produce a non-negligible amount of noise in our measurement of the SZ signal (see Section 9.2). Using a rigorous decision tree based on application of the F-test, we find that a physically-motivated model composed of a *Chandra*-derived pseudo Compton- y map to describe

the thermal SZ signal, plus an additional template centered on sub-cluster B with different normalizations at 140 and 268 GHz, is the minimum model that is adequate to describe our data. We note that sub-cluster B has a measured spectroscopic line-of-sight velocity of $+3200 \text{ km s}^{-1}$ (Ma et al. 2009).

From this best-fit model, we compute the two-band SZ surface brightness toward sub-cluster B, along with the most massive sub-cluster, C. We also compute the SZ surface brightness by directly integrating the Bolocam images, although the best-fit model is required to constrain the DC signal level of these images, which is filtered away by our data processing. For both the model-derived and directly integrated SZ surface brightnesses, we include uncertainties due to measurement noise and absolute flux calibration. In addition, we include an uncertainty due to the variations in derived surface brightnesses for a range of physically motivated models that we could have chosen to describe our data, and we find that this uncertainty is similar to our measurement uncertainty.

Using our measured SZ surface brightnesses toward sub-clusters B and C, along with our X-ray-derived electron temperatures for each sub-cluster, we constrain a spectral model consisting of thermal and kinetic SZ components (see Figure 6). For these fits, we assume that the ICM is isothermal within small apertures centered on each sub-cluster, and we include corrections for relativistic effects. We find that a thermal SZ signal is adequate to describe the SZ surface brightnesses of sub-cluster C, but that an additional kinetic SZ signal is required for sub-cluster B. From our model-derived SZ surface brightnesses, this kinetic SZ signal implies a line-of-sight velocity of $v_z = +3450 \text{ km s}^{-1}$, while the directly integrated SZ surface brightnesses imply a line-of-sight velocity of $v_z = +2550 \text{ km s}^{-1}$, both of which are in good agreement with the spectroscopic measurement of Ma et al. (2009, See Figure 5). From the model fit we find that $(1 - \text{Prob}[v_z \geq 0])$ is 1.3×10^{-5} , which corresponds to being 4.2σ from 0 for a Gaussian distribution. Similarly, from the direct integration of the SZ surface brightness, we find that $(1 - \text{Prob}[v_z \geq 0])$ is 2.2×10^{-3} , which corresponds to being 2.9σ from 0 for a Gaussian distribution.

We consider potential biases in our derived values of v_z due to possible systematics in the X-ray derived T_e , and due to merger and projection effects as a result of the complex dynamics of this cluster, and we find that neither bias is likely to be significant compared to our measurement uncertainties. We find that raw SZ mea-

surement sensitivity limits our constraints on v_z , and uncertainties from the X-ray data, the CIB, the CMB, and flux calibration are sub-dominant, although deeper SZ measurements will likely be limited by some combination of these factors. Our data, combined with the results from Ma et al. (2009), indicate that sub-cluster B is moving with a line-of-sight velocity of $\simeq +3000 \text{ km s}^{-1}$, a value that is high, but not in tension with standard cosmological models.

11. ACKNOWLEDGMENTS

We acknowledge the assistance of: the day crew and Hilo staff of the Caltech Submillimeter Observatory, who provided invaluable assistance during data-taking for this data set; Kathy Deniston, Barbara Wertz, and Diana Bisel, who provided effective administrative support at Caltech and in Hilo; the Bolocam observations were partially supported by the Gordon and Betty Moore Foundation. JS was supported by NSF/AST-0838261, NASA/NNX11AB07G, and the Norris Foundation CCAT Postdoctoral Fellowship; support for TM was provided by NASA through Einstein Fellowship Program grant number PF0-110077 awarded by the *Chandra* X-ray Center, which is operated by the Smithsonian Astrophysical Observatory for NASA under contract NAS8-03060; PMK was supported by a NASA Postdoctoral Program Fellowship; NC was partially supported by a NASA Graduate Student Research Fellowship; AM was partially supported by NSF/AST-0838187 and NSF/AST-1140019; EP and JAS were partially supported by NASA/NNX07AH59G; SS was supported by NASA Earth and Space Science Fellowship NASA/NNX12AL62H; KU acknowledges partial support from the National Science Council of Taiwan grant NSC100-2112-M-001-008-MY3 and from the Academia Sinica Career Development Award. A portion of this research was carried out at the Jet Propulsion Laboratory, California Institute of Technology, under a contract with the National Aeronautics and Space Administration. This research made use of the Caltech Submillimeter Observatory, which was operated at the time by the California Institute of Technology under cooperative agreement with the National Science Foundation (NSF/AST-0838261). This work is based in part on observations made with *Herschel*, a European Space Agency Cornerstone Mission with a significant participation by NASA. Partial support for this work was provided by NASA through an award issued by JPL/Caltech.

Facilities: CSO, *Chandra*, *Herschel*-SPIRE, *XMM-Newton*.

REFERENCES

- Arnaud, M., Pratt, G. W., Piffaretti, R., Böhringer, H., Croston, J. H., & Pointecouteau, E. 2010, *A&A*, 517, A92
Austermann, J. E., et al. 2009, *MNRAS*, 393, 1573
Bai, L., et al. 2007, *ApJ*, 664, 181
Bennett, C. L., et al. 2012, arXiv:1212.5225
Benson, B. A., et al. 2003, *ApJ*, 592, 674
Béthermin, M., Dole, H., Lagache, G., Le Borgne, D., & Penin, A. 2011, *A&A*, 529, A4
Bhattacharya, S., & Kosowsky, A. 2008, *Phys. Rev. D*, 77, 083004
Birkinshaw, M. 1999, *Phys. Rep.*, 310, 97
Blain, A. W., Smail, I., Ivison, R. J., Kneib, J.-P., & Frayer, D. T. 2002, *Phys. Rep.*, 369, 111
Bonafede, A., et al. 2009, *A&A*, 503, 707
Bulbul, G. E., Smith, R. K., Foster, A., Cottam, J., Loewenstein, M., Mushotzky, R., & Shafer, R. 2012, *ApJ*, 747, 32
Carlstrom, J. E., Holder, G. P., & Reese, E. D. 2002, *ARA&A*, 40, 643
Chluba, J., Nagai, D., Sazonov, S., & Nelson, K. 2012, *MNRAS*, 426, 510
Conley, A., et al. 2011, *ApJS*, 192, 1
Czakon, N. G. 2013, *in prep*
Dorman, B., & Arnaud, K. A. 2001, in *Astronomical Society of the Pacific Conference Series*, Vol. 238, *Astronomical Data Analysis Software and Systems X*, ed. F. R. Harnden, Jr., F. A. Primini, & H. E. Payne, 415
Downes, T. P. 2009, PhD thesis, University of Chicago

- Downes, T. P., Welch, D., Scott, K. S., Austermann, J., Wilson, G. W., & Yun, M. S. 2012, *MNRAS*, 423, 529
- Ebeling, H., Barrett, E., & Donovan, D. 2004, *ApJ*, 609, L49
- Ebeling, H., Barrett, E., Donovan, D., Ma, C.-J., Edge, A. C., & van Speybroeck, L. 2007, *ApJ*, 661, L33
- Ebeling, H., Edge, A. C., & Henry, J. P. 2001, *ApJ*, 553, 668
- Edge, A. C., Ebeling, H., Bremer, M., Röttgering, H., van Haarlem, M. P., Rengelink, R., & Courtney, N. J. D. 2003, *MNRAS*, 339, 913
- Feldman, H. A., Watkins, R., & Hudson, M. J. 2010, *MNRAS*, 407, 2328
- Finn, R. A., et al. 2010, *ApJ*, 720, 87
- Fruscione, A., et al. 2006, in *Society of Photo-Optical Instrumentation Engineers (SPIE) Conference Series*, Vol. 6270, *Society of Photo-Optical Instrumentation Engineers (SPIE) Conference Series*
- Geach, J. E., et al. 2006, *ApJ*, 649, 661
- Glenn, J., et al. 2002, in *Astronomical Society of the Pacific Conference Series*, Vol. 283, *A New Era in Cosmology*, ed. N. Metcalfe & T. Shanks, 398
- Griffin, M. J., & Orton, G. S. 1993, *Icarus*, 105, 537
- Haig, D. J., et al. 2004, in *Society of Photo-Optical Instrumentation Engineers (SPIE) Conference Series*, Vol. 5498, *Society of Photo-Optical Instrumentation Engineers (SPIE) Conference Series*, ed. C. M. Bradford, P. A. R. Ade, J. E. Aguirre, J. J. Bock, M. Dragovan, L. Duband, L. Earle, J. Glenn, H. Matsuhara, B. J. Naylor, H. T. Nguyen, M. Yun, & J. Zmuidzinas, 78–94
- Hall, N. R., et al. 2010, *ApJ*, 718, 632
- Hand, N., et al. 2012, *Physical Review Letters*, 109, 041101
- Hasselfield, M., et al. 2013, arXiv:1303.4714
- Hayashi, E., & White, S. D. M. 2006, *MNRAS*, 370, L38
- Hinshaw, G., et al. 2012, arXiv:1212.5226
- Holzzapfel, W. L., Ade, P. A. R., Church, S. E., Mauskopf, P. D., Rephaeli, Y., Wilbanks, T. M., & Lange, A. E. 1997, *ApJ*, 481, 35
- Itoh, N., Kohyama, Y., & Nozawa, S. 1998, *ApJ*, 502, 7
- Itoh, N., & Nozawa, S. 2004, *A&A*, 417, 827
- Jauzac, M., et al. 2012, *MNRAS*, 426, 3369
- Kitayama, T., Komatsu, E., Ota, N., Kuwabara, T., Suto, Y., Yoshikawa, K., Hattori, M., & Matsuo, H. 2004, *PASJ*, 56, 17
- Kosowsky, A., & Bhattacharya, S. 2009, *Phys. Rev. D*, 80, 062003
- Kuntz, K. D., & Snowden, S. L. 2008, *ApJ*, 674, 209
- Lee, J., & Komatsu, E. 2010, *ApJ*, 718, 60
- Levenson, L., et al. 2010, *MNRAS*, 409, 83
- Li, C. K., Jia, S. M., Chen, Y., Xiang, F., Wang, Y. S., & Zhao, H. H. 2012, *A&A*, 545, A100
- Limousin, M., et al. 2012, *A&A*, 544, A71
- Ma, C.-J., Ebeling, H., & Barrett, E. 2009, *ApJ*, 693, L56
- Ma, Y.-Z., Branchini, E., & Scott, D. 2012, *MNRAS*, 425, 2880
- Mahdavi, A., Hoekstra, H., Babul, A., Bildfell, C., Jeltama, T., & Henry, J. P. 2013, *ApJ*, 767, 116
- Mak, D. S. Y., Pierpaoli, E., & Osborne, S. J. 2011, *ApJ*, 736, 116
- Mantz, A., Allen, S. W., Ebeling, H., Rapetti, D., & Drlica-Wagner, A. 2010, *MNRAS*, 406, 1773
- Marcillac, D., Rigby, J. R., Rieke, G. H., & Kelly, D. M. 2007, *ApJ*, 654, 825
- Markwardt, C. B. 2009, in *Astronomical Society of the Pacific Conference Series*, Vol. 411, *Astronomical Data Analysis Software and Systems XVIII*, ed. D. A. Bohlender, D. Durand, & P. Dowler, 251
- Mauskopf, P. D., et al. 2012, *MNRAS*, 421, 224
- Medzinski, E., et al. 2013, arXiv:1304.1223
- Meneghetti, M., Fedeli, C., Zitrin, A., Bartelmann, M., Broadhurst, T., Gottlöber, S., Moscardini, L., & Yepes, G. 2011, *A&A*, 530, A17
- Mroczkowski, T., et al. 2012, *ApJ*, 761, 47
- Nevalainen, J., David, L., & Guainazzi, M. 2010, *A&A*, 523, A22
- Nguyen, H. T., et al. 2010, *A&A*, 518, L5
- Nozawa, S., Itoh, N., & Kohyama, Y. 1998a, *ApJ*, 508, 17
- 1998b, *ApJ*, 507, 530
- Nozawa, S., Itoh, N., Suda, Y., & Ohhata, Y. 2006, *Nuovo Cimento B Serie*, 121, 487
- Nusser, A., & Davis, M. 2011, *ApJ*, 736, 93
- Osborne, S. J., Mak, D. S. Y., Church, S. E., & Pierpaoli, E. 2011, *ApJ*, 737, 98
- Ott, S. 2010, in *Astronomical Society of the Pacific Conference Series*, Vol. 434, *Astronomical Data Analysis Software and Systems XIX*, ed. Y. Mizumoto, K.-I. Morita, & M. Ohishi, 139
- Ott, S., et al. 2006, in *Astronomical Society of the Pacific Conference Series*, Vol. 351, *Astronomical Data Analysis Software and Systems XV*, ed. C. Gabriel, C. Arviset, D. Ponz, & S. Enrique, 516
- Planck Collaboration et al. 2013a, arXiv:1303.5069
- 2013b, arXiv:1303.5075
- 2013c, arXiv:1303.5076
- 2013d, arXiv:1303.5090
- Prokhorov, D. A., & Colafrancesco, S. 2012, *MNRAS*, 424, L49
- Rawle, T. D., et al. 2012, *ApJ*, 747, 29
- Reese, E. D., Kawahara, H., Kitayama, T., Ota, N., Sasaki, S., & Suto, Y. 2010, *ApJ*, 721, 653
- Reichardt, C. L., et al. 2012, *ApJ*, 755, 70
- Rephaeli, Y. 1995a, *ARA&A*, 33, 541
- 1995b, *ApJ*, 445, 33
- Roseboom, I. G., et al. 2013, arXiv:1308.4443
- Ruan, J. J., Quinn, T. R., & Babul, A. 2013, *MNRAS*
- Sanders, J. S. 2006, *MNRAS*, 371, 829
- Sayers, J., Czakon, N. G., & Golwala, S. R. 2012, *ApJ*, 744, 169
- Sayers, J., et al. 2013a, *ApJ*, 768, 177
- Sayers, J., Golwala, S. R., Ameglio, S., & Pierpaoli, E. 2011, *ApJ*, 728, 39
- Sayers, J., et al. 2013b, *ApJ*, 764, 152
- Sazonov, S. Y., & Sunyaev, R. A. 1998, *ApJ*, 508, 1
- Smith, A. J., et al. 2012, *MNRAS*, 419, 377
- Smith, R. K., Brickhouse, N. S., Liedahl, D. A., & Raymond, J. C. 2001, *ApJ*, 556, L91
- Snowden, S. L., Mushotzky, R. F., Kuntz, K. D., & Davis, D. S. 2008, *A&A*, 478, 615
- Story, K. T., et al. 2012, arXiv:1210.7231
- Sunyaev, R. A., & Zel'dovich, Y. B. 1972, *Comments on Astrophysics and Space Physics*, 4, 173
- Suzuki, N., et al. 2012, *ApJ*, 746, 85
- Thompson, R., & Nagamine, K. 2012, *MNRAS*, 419, 3560
- Tully, R. B., & Fisher, J. R. 1977, *A&A*, 54, 661
- van Weeren, R. J., Röttgering, H. J. A., Brüggén, M., & Cohen, A. 2009, *A&A*, 505, 991
- Viero, M. P., et al. 2013, *ApJ*, 772, 77
- Waizmann, J.-C., Redlich, M., & Bartelmann, M. 2012, *A&A*, 547, A67
- Wardlow, J. L., et al. 2010, *MNRAS*, 401, 2299
- Weiland, J. L., et al. 2011, *ApJS*, 192, 19
- Wu, J., et al. 2012, *ApJ*, 756, 96
- Zahn, O., et al. 2012, *ApJ*, 756, 65
- Zemcov, M., et al. 2012, *ApJ*, 749, 114
- 2013, *ApJ*, 769, L31
- Zhuravleva, I., Churazov, E., Kravtsov, A., Lau, E. T., Nagai, D., & Sunyaev, R. 2013, *MNRAS*, 428, 3274
- Zitrin, A., Broadhurst, T., Rephaeli, Y., & Sadeh, S. 2009, *ApJ*, 707, L102

APPENDIX

There is a significant amount of signal from unresolved dusty star-forming galaxies (e.g., Blain et al. 2002) in our 268 GHz Bolocam map, and we describe our treatment of these galaxies in this Appendix. Unlike the resolved SZ signal we seek to measure, all of the dusty star-forming galaxies in our Bolocam image are unresolved. Therefore, to maximize our sensitivity to these unresolved sources, we process the 268 GHz data using an adaptive principal component analysis (PCA) algorithm in place of the common-mode subtraction we use for our SZ analysis. For brevity, we refer to the

maps generated by these reductions as the adaptive-PCA map and the common-mode-subtraction map. The details of the adaptive-PCA algorithm we use for this analysis are given in Wu et al. (2012). This processing results in an adaptive-PCA map with a noise rms of 0.7 mJy/beam, which is approximately equal to the confusion noise from unresolved star-forming galaxies. We then subtract a template of the extended SZ signal from the adaptive-PCA map by fitting a gNFW profile to the common-mode-subtraction map, processing the gNFW model through the adaptive-PCA reduction, and subtracting the processed model from the adaptive-PCA map (see Figure 7). The resulting extended-SZ-subtracted adaptive-PCA map contains a total of 8 unresolved galaxy candidates with a S/N > 4, and we measure the best-fit flux density for each of these candidates after accounting for the filtering effects of the adaptive-PCA reduction (see Table 4). Using these best-fit flux densities and positions, we then process these 8 candidates through the common-mode reduction and subtract them from the common-mode-subtraction map used for our SZ analysis. In addition, we generate 1000 random realizations of each of the 8 candidates based on the measurement uncertainties on the best-fit flux densities, and we add one realization of the uncertainty for each candidate to each of the 1000 noise realizations described in Section 4.1.

In addition to our Bolocam data, we also search for dusty star-forming galaxies in three-band (250, 350, and 500 μm) observations obtained with the SPIRE photometer. All of the SPIRE images are dominated by confusion noise from unresolved galaxies (Nguyen et al. 2010), and the effective rms is 7.2, 5.3, and 5.8 mJy/beam at 250, 350, and 500 μm . The SPIRE data are reduced using the *Herschel* Interactive Processing Environment HIPE (Ott et al. 2006; Ott 2010), along with the HerMES SMAP package (Levenson et al. 2010; Viero et al. 2013). Source catalogs are then compiled using the SCAT procedure (Smith et al. 2012), and we identify a total of 200 source candidates within the $14' \times 14'$ Bolocam coverage with S/N > 3 in any of the SPIRE bands. We note that very few of the SPIRE detections are located within the extended SZ signal detected with Bolocam, and none of the sources located within the extended SZ signal are particularly bright, indicating that there is little contamination of the extended SZ signal due to bright dusty star-forming galaxies.

For each candidate SPIRE galaxy we fit the three-band SPIRE data to a greybody spectral energy distribution of the form

$$S(\nu) = A \times \nu^{1.7} \times B(\nu, T), \quad (1)$$

where $B(\nu, T)$ is the Planck blackbody equation and the normalization A and temperature T are free parameters. In performing these fits, we make the assumption that this greybody parameterization describes the emission within the SPIRE PSF regardless of whether the emission is sourced by a single galaxy or many galaxies. Consequently, we do not include the effects of confusion noise in these fits. Using the greybody fits to the SPIRE data, we estimate the 268 GHz flux density centered on each of the 200 SPIRE candidates. We note that, probably due to the fact that multiple sources above the SPIRE measurement noise RMS are likely to be present within the extent of the SPIRE PSF, this simple greybody model does not provide an adequate fit to all of the SPIRE source candidates. Specifically, 1/3 of candidates produce a fit PTE < 0.05, indicating that a greybody fit does not describe the emission detected within the SPIRE PSF for those candidates. In addition, even if we discard these 1/3 of the candidates, the distribution of PTE values for the remaining 2/3 of the candidates is still marginally inconsistent with a uniform distribution, quantified by a KS test PTE of 0.03. This implies that a greybody fit is inadequate to describe a significant fraction of the SPIRE candidates. Unfortunately, it is not practical to fit a more complicated model to the 3-band SPIRE data alone due to the lack of spectral information, and so there is no clear model extension to obtain a better fit quality for the SPIRE candidates that are not adequately described using a greybody model. We discuss the implications of this modeling limitation in more detail below.

We find a total of 14 of these SPIRE candidates are located within $30''$ of the 8 Bolocam candidates, indicating that they are possible counterparts. To compare the Bolocam and SPIRE measurements, we first estimate the best-fit noise-de-boosted flux density for the 8 candidates detected by Bolocam according to the AzTEC de-boosting algorithm presented in Austermann et al. (2009) by interpolating the tabulated values presented in Downes et al. (2012). As shown in Figure 8 and Table 4, we in general find good agreement between the de-boosted Bolocam flux densities and the sum of the extrapolated SPIRE flux densities for all of the likely counterparts. Therefore, the Bolocam candidates are robust detections.

Discarding the 14 SPIRE candidates that are likely counterparts of the Bolocam candidates because they have already been subtracted from the common-mode-subtraction map, along with 24 SPIRE candidates that have an extrapolated 268 GHz S/N < 2, we then generate an image from the remaining 162 SPIRE candidates using the extrapolated 268 GHz SPIRE flux densities convolved with the Bolocam PSF. This image is then processed through the adaptive-PCA reduction, and we subtract it from the corresponding extended-SZ-and-Bolocam-candidate-subtracted adaptive-PCA map (see Figure 7). Removal of this SPIRE template, which we generate independently from our Bolocam data, results in a significant reduction in the rms of the Bolocam image, with a $\Delta\chi^2 = 166$. To put this value in context, the total χ^2 of the SPIRE template is 240, and therefore a perfect correlation between the SPIRE extrapolations and the Bolocam data would have resulted in a $\Delta\chi^2 = 240$. As a further quality check, we compute the normalization of the SPIRE template that best fits our 268 GHz Bolocam extended-SZ-and-Bolocam-candidate-subtracted adaptive-PCA map and find a value of 0.84 ± 0.09 including flux calibration uncertainties. The consistency of this value with unity indicates that the SPIRE template is a good description of the CIB in the 268 GHz Bolocam data.

To subtract these 162 SPIRE-detected sources from our common-mode-subtraction map, we process the SPIRE template through the common-mode reduction and subtract the resulting map from the corresponding common-mode-subtraction map we use for SZ analysis. We also generate 1000 map realizations with flux densities for each source

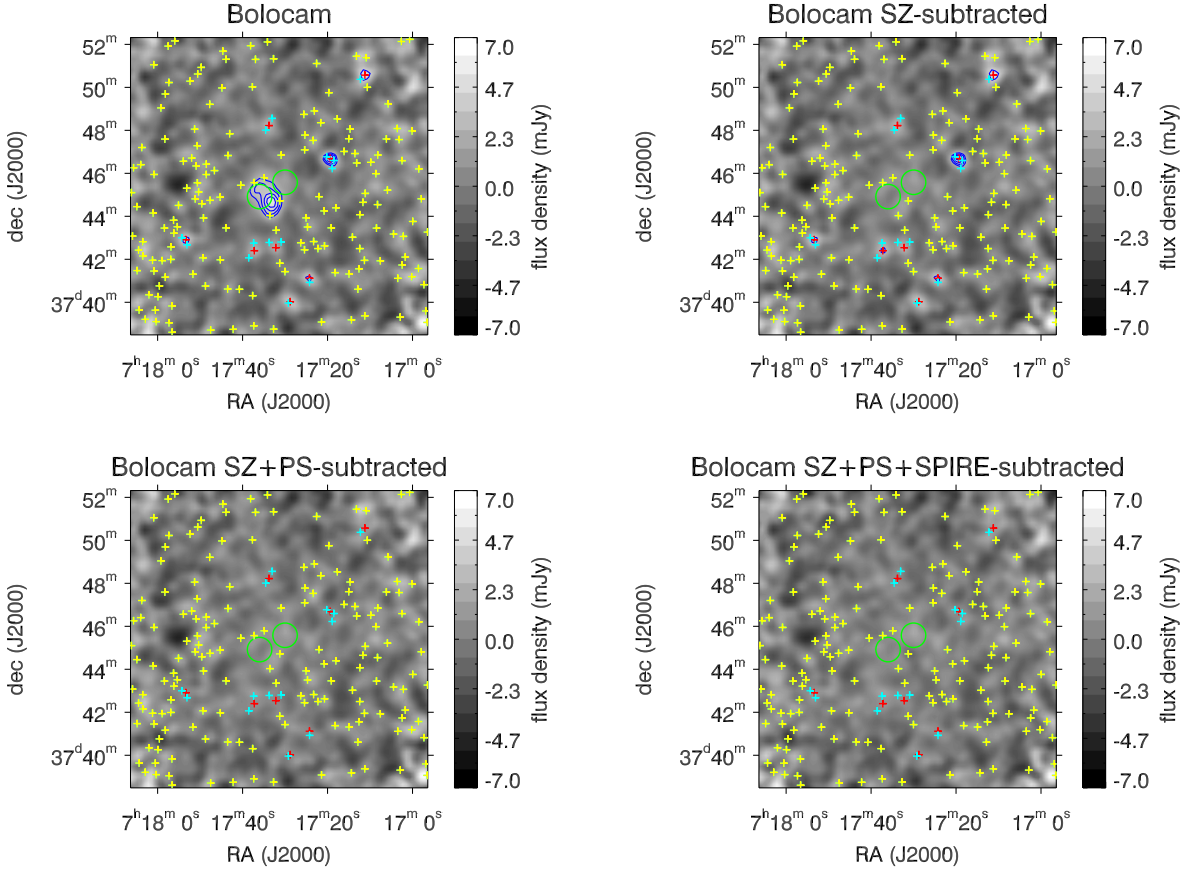


FIG. 7.— Bolocam 268 GHz images we obtain from the adaptive-PCA reduction. Clockwise from upper left: nominal image, image after subtracting the best-fit extended-SZ template, image after also subtracting the 8 unresolved sources detected by Bolocam, and image after also subtracting the 162 sources detected by SPIRE and extrapolated to Bolocam’s band using a greybody fit. The blue contours show S/N, starting at 4 and separated by 1. There are no contours around the bright regions in the corners of the images, due to the higher noise in these regions as a result of reduced integration time relative to the central region. Note that even in this heavily filtered image, an extended SZ signal is detected at high significance. The crosses show: Bolocam detections (red), likely SPIRE counterparts to those detections (cyan), and all other SPIRE detections with an extrapolated S/N > 2 (yellow). The green circles show the 1’ diameter apertures centered on sub-cluster C (lower left) and sub-cluster B (upper right).

TABLE 4
UNRESOLVED SOURCES DETECTED BY BOLOCAM AT 268 GHz

RA (J2000)	dec (J2000)	flux density (mJy)	de-boosted (mJy)	SPIRE extrapolated (mJy)	SPIRE distance (’)
7:17:19.4	37:46:41	7.6 ± 0.9	6.9 ± 0.8	6.2 ± 0.5	11
				1.6 ± 0.2	11
				0.4 ± 0.1	28
7:17:53.4	37:42:55	5.2 ± 1.2	3.7 ± 1.4	2.2 ± 0.1	12
				1.4 ± 0.1	15
				3.7 ± 0.6	11
7:17:24.3	37:41:07	5.3 ± 1.1	4.0 ± 1.2	1.2 ± 0.1	21
				2.5 ± 0.5	25
				0.5 ± 0.1	22
7:17:37.3	37:42:24	3.9 ± 0.9	3.2 ± 1.0	0.8 ± 0.1	23
				3.0 ± 0.1	17
				5.3 ± 0.3	7
7:17:32.2	37:42:32	3.6 ± 0.9	3.0 ± 1.0	2.9 ± 0.5	16
				0.6 ± 0.1	22
				3.5 ± 0.9	16
7:17:11.2	37:50:34	6.3 ± 1.4	4.0 ± 1.7	3.0 ± 0.1	17
				5.3 ± 0.3	7
				2.9 ± 0.5	16
7:17:28.8	37:40:02	5.3 ± 1.3	3.5 ± 1.6	0.6 ± 0.1	22
				2.9 ± 0.5	16
				0.6 ± 0.1	22
7:17:33.8	37:48:13	3.5 ± 0.9	2.9 ± 1.0	0.6 ± 0.1	22
				0.6 ± 0.1	22
				0.6 ± 0.1	22

NOTE. — Unresolved sources that we detect with a S/N ≥ 4 in the Bolocam 268 GHz data. From left to right, the columns give the Bolocam RA, Bolocam dec, Bolocam flux density, noise-de-boosted Bolocam flux density, extrapolated flux density at 268 GHz based on our greybody fit to measurements from the 3 SPIRE bands, and distance from the Bolocam detection to the SPIRE detection. Note that the SPIRE measurements are dominated by confusion noise, which is highly correlated between the bands and is not included in the greybody fit uncertainties. Consequently, the uncertainties on the greybody fits assume that there is either a single source contributing all of the signal in the three SPIRE bands, or that the superposition of sources can be adequately described by a single greybody. For each of these eight candidate sources, the sum of the SPIRE greybody fits is consistent with the de-boosted Bolocam flux density, indicating that the Bolocam candidates are likely robust detections.

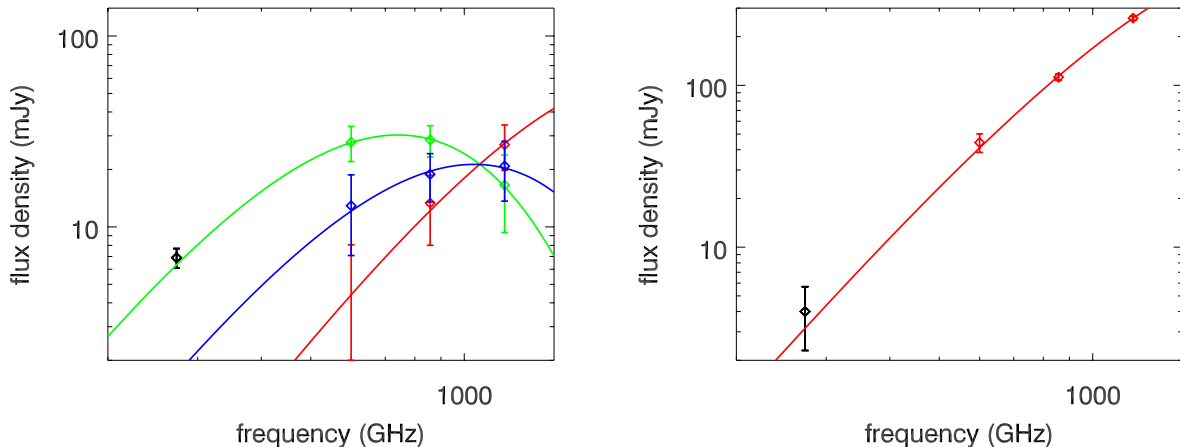


FIG. 8.— Two of the eight candidate galaxies detected by Bolocam. In each plot the de-boosted Bolocam flux density is shown as a black diamond, and the SPIRE flux densities are shown as colored diamonds with a different color for each possible counterpart. The lines show greybody SED fits to the SPIRE data only, with a separate fit for each possible counterpart.

randomly distributed according to the uncertainty on the extrapolation and add one such realization to each of the 1000 noise realizations. As described above, the likely Bolocam counterparts are not included in this SPIRE-source template to avoid potential double subtractions, and the $S/N < 2$ extrapolations are removed to prevent the subtraction of possible false SPIRE detections. We estimate that, between the Bolocam and SPIRE detections, we remove all of the dusty galaxies with a 268 GHz flux density $\gtrsim 1$ mJy along with $\simeq 100$ galaxies with lower flux densities, significantly reducing the contamination from these sources on our measurement of the SZ signal (see Figure 9, left).

Due to the fact that the SPIRE candidates are in general not well described by the greybody model, the derived uncertainty on the extrapolation is likely to be underestimated. Therefore, to determine the effect that this underestimate might have on our SZ results, we artificially increase the uncertainties on the SPIRE photometry for each candidate until the reduced χ^2 of the greybody fit is equal to 1. For candidates with a reduced $\chi^2 < 1$, the uncertainties are left unchanged. Although this procedure is unphysical, it does provide a reasonable basis for estimating the uncertainty on the extrapolation for these sources. We find that the difference between the estimated uncertainties on the 268 GHz SZ brightnesses for sub-clusters B and C with and without including this artificial increase on the extrapolation uncertainty is $< 4 \times 10^{-4}$ MJy sr $^{-1}$, or $\lesssim 1\%$ of the nominal uncertainties. Therefore, we have not accounted for the potentially underestimated uncertainties on the SPIRE candidates that are poorly fit by the greybody model.

In addition, we also estimate the uncertainty on the extrapolation due to our particular choice of greybody model. Specifically, we fixed the spectral index of the greybody to 1.7, while the measured spectral indices from large source catalogs vary between $\simeq 1-2$ (e.g., Roseboom et al. 2013). To bound the maximum possible change in the extrapolated CIB template due to this source variation, we reran our analysis using spectral indices of 1.1 and 2.1, which correspond to the 1σ bounds determined by Roseboom et al. (2013). Using the templates determined from these spectral indices, the 268 GHz SZ brightnesses toward sub-clusters B and C change by 0.001 – 0.005 MJy sr $^{-1}$, or by as much as 10% of their nominal uncertainties. When added in quadrature with our overall uncertainties this amount is negligible, and we therefore have not included it in our uncertainty estimates.

Furthermore, we note that the best-fit amplitude of our nominal CIB template using Bolocam data is 0.84 ± 0.09 , hinting that the SPIRE data may be producing a template that is slightly over-predicting the CIB at 268 GHz. This could be caused by, for example, noise-boosted flux densities in the SPIRE data or an incorrect choice of SED template. To estimate the effects of such a potential bias, we re-estimated the 268 GHz SZ brightnesses of sub-clusters B and C after subtracting an extrapolated SPIRE template with the best-fit Bolocam normalization of 0.84 (rather than 1). Using this renormalized template results in SZ brightnesses that differ by $\lesssim 0.001$ MJy sr $^{-1}$ compared to those found with the default normalization of the template, or by approximately 2% of our nominal uncertainties. Therefore, the bias associated with a potential over-estimate of the CIB template is negligible, and we have not attempted to account for such a bias in our analysis.

Bolocam and SPIRE do not individually detect the faint galaxies that comprise most of the CIB. Consequently, we use the CIB model determined by Béthermin et al. (2011) to account for the noise fluctuations from these undetected galaxies, as it provides a reasonable estimate for the behavior of the component of the CIB below the SPIRE detection limit. We model the undetected CIB using a number counts distribution obtained by subtracting the number counts already detected by SPIRE and Bolocam from the Béthermin et al. (2011) number counts model. We then generate 1000 random sky realizations of the sources in this population, process each such realization through the common-mode reduction, and add one realization of this faint CIB model to each of our 1000 noise realizations.

We note that the Béthermin et al. (2011) model was calibrated using observations of blank sky and therefore is not necessarily an accurate description of the CIB toward a massive cluster like MACS J0717.5+3745. Although the emission from cluster-member galaxies at 268 GHz is likely to be negligible compared to the background CIB,¹⁸ the

¹⁸ For example, see the arguments presented in Section 4 of Sayers et al. (2013b) based on the results presented in Geach et al.

(2006); Bai et al. (2007); Marcillac et al. (2007); Finn et al. (2010); Rawle et al. (2012).

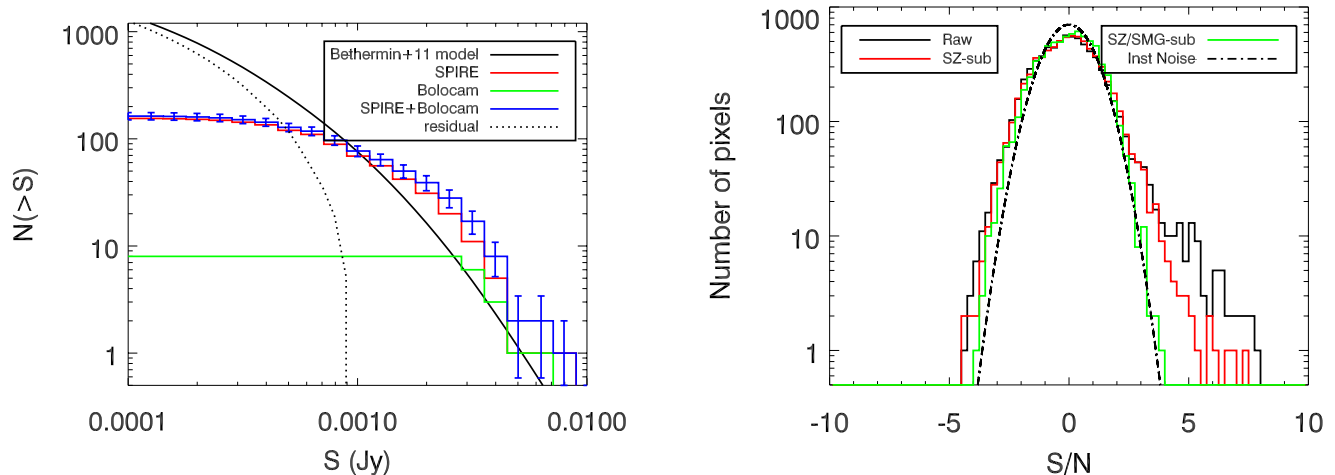


FIG. 9.— Left: number of galaxies above a given 268 GHz flux density within the $14' \times 14'$ Bolocam image. The solid black line denotes the Béthermin et al. (2011) model prediction, green denotes the Bolocam detections, red denotes the extrapolated SPIRE detections after removing possible counterparts to the Bolocam detections along with $S/N < 2$ extrapolations, blue denotes all Bolocam and SPIRE detections, and the dashed black line is the difference between the model and our total detections. Right: S/N histogram for the 268 GHz Bolocam adaptive-PCA map. Black shows the histogram prior to any signal subtraction, red shows the histogram after subtraction of the best-fit extended-SZ model, green shows the histogram after further subtraction of the eight sources detected by Bolocam and the 162 sources detected by SPIRE and extrapolated to 268 GHz, and the dot-dashed black line shows the histogram of our jackknife realizations, which contain all of the non-astronomical noise present in our data. The difference in width between the green histogram and the dot-dashed black histogram matches the prediction of the Béthermin et al. (2011) model, indicating that it provides an adequate description of our data.

significant magnification of the background due to gravitational lensing can distort the number counts. In particular, lensing preserves the total surface brightness of the CIB, but causes a significant and spatially dependent change in the number counts (Zemcov et al. 2013). Our data show hints of this change as an excess of sources at bright flux densities, which is consistent with measurements toward massive clusters using AzTEC at the same wavelength (Wardlow et al. 2010; Downes 2009). It is therefore not clear how well the unlensed Béthermin et al. (2011) model describes the faint population of dusty star-forming galaxies toward MACS J0717.5+3745.

To test the validity of the Béthermin et al. (2011) model in describing our MACS J0717.5+3745 data, we add a random sky realization to each jackknife realization of the adaptive-PCA map, where the sky realizations are based on the aforementioned difference between the Béthermin et al. (2011) model and our detected number counts. We find that adding these random sky realizations increases the noise rms by 12.3%. We then fit a Gaussian to the distributions of pixel S/N values for the adaptive-PCA map jackknife realizations, and to the actual data after subtraction of the extended-SZ template, the Bolocam detections, and the extrapolated SPIRE detections (see Figure 9, right). We find that the Gaussian standard deviations returned by the fits differ by $11.9 \pm 0.8\%$, in excellent agreement with the prediction based on the Béthermin et al. (2011) model. Therefore, the Béthermin et al. (2011) model provides a good description of the global noise fluctuations due to dim unresolved galaxies at the level we are able to ascertain with our Bolocam data.

In principal, we could subtract some of the signal from these dim unresolved galaxies via e.g., a cross correlation analysis between the SPIRE and Bolocam maps. Although these dim galaxies are not detected in any single SPIRE band, their signal will be correlated across the ensemble of SPIRE and Bolocam bands. However, the SPIRE data, particularly at $500 \mu\text{m}$, contains a non-negligible amount of diffuse SZ signal. This signal would also be correlated across the multiple bands, and therefore such an analysis could subtract SZ signal from the Bolocam data in addition to CIB signal. Furthermore, the effective reddening of the CIB due to the SZ signal in the SPIRE data could potentially cause a significant over-estimate of the signal when extrapolated to the Bolocam bands. Consequently, to mitigate these effects, we have chosen to subtract only the unresolved bright galaxies individually detected by SPIRE, which should not be significantly contaminated by the diffuse SZ signal. Although beyond the scope of this work, an optimal analysis would jointly constrain a model of the SZ and CIB signals via a simultaneous fit to both the SPIRE and Bolocam data. However, given the relative dimness of the SZ signal in the SPIRE bands, along with the relative dimness of the CIB signal in the Bolocam bands, the improvement from such a joint fit is likely to be minimal compared to our analysis procedure.

We note that the fluctuations from the CIB are accounted for in our 140 GHz data by adding noise realizations generated according to the power spectrum measurements from SPT (Hall et al. 2010). We do not attempt to subtract any individual galaxies due to the large, and consequently potentially untrustworthy, spectral extrapolation that would be required from the SPIRE measurements. In addition, as noted above, there are very few galaxies detected within the extended region containing bright SZ signal, and none of those galaxies are particularly bright. We note that this is in general true for massive clusters, as shown in Zemcov et al. (2013). However, to verify that the CIB is sufficiently dim that we can neglect subtracting it at 140 GHz, we extrapolated the SPIRE detections to 140 GHz and removed them from the Bolocam data. Even if this large extrapolation is potentially untrustworthy, it should provide a reasonable estimate of the potential brightness of the CIB at 140 GHz. When we subtract this extrapolated CIB, we find that

the best-fit 140 GHz SZ brightnesses toward both sub-cluster B and sub-cluster C changes by $\simeq 5 \times 10^{-4}$ MJy sr $^{-1}$, or by approximately 1% of the total uncertainty on each sub-cluster's SZ brightness. Therefore, neglecting to subtract the CIB at 140 GHz has a negligible effect on our overall results.